GEOPHYSICS, VOL. 47, NO. 3 (MARCH 1982); P. 345–353, 13 FIGS., 2 TABLES.



# Acoustic wave propagation in air-bubble curtains in water—Part I: History and theory

S. N. Domenico*


## ABSTRACT

Air bubbles in water increase the compressibility several orders of magnitude above that in bubble-free water, thereby greatly reducing the velocity and increasing attenuation of acoustic waves. The effect of air bubbles in water on acoustic wave propagation was studied extensively during World War II as part of an overall effort to apply underwater sound in submarine warfare. Currently, air bubble curtains are used to prevent damage of submerged structures (e.g., dams) by shock waves from submarine explosives. Also, air-bubble curtains are used to reduce damage to water-filled tanks in which metals are formed by explosives.

Since World War II, research has progressed less feverishly in government and university laboratories. Published results of laboratory experiments generally confirm theoretical velocity and attenuation functions and demonstrate that these quantities are dependent principally upon frequency, bubble size, and fractional volume of air. Below the bubble resonant frequency and in the frequency range of marine energy sources, acoustic wave velocity is essentially independent of frequency and bubble radius, being well below the velocity in bubble-free water. In this frequency range, attenuation increases with increasing frequency, decreasing bubble radius, and increasing fractional air volume.


## INTRODUCTION

A small fractional volume (0.01 and less) of air bubbles in water or, more generally, gaseous bubbles in a fluid, can reduce acoustic wave velocity and increase attenuation orders of magnitude from values for a gas-free fluid. In this paper, a brief review of previously proposed and present applications of air-bubble curtains in water is given, followed by a description of the theory and experimental verification of sound attenuation and velocity in such a mixture. Finally, theoretical velocity and attenuation functions are developed for specific physical parameters (temperature, water salinity, density, etc.) representative of those at the test site of a field experiment described in Domenico (1982, this issue).

## PREVIOUS AND PRESENT APPLICATIONS

Possibly the first practical application of the pronounced attenuating property of air bubbles in water was one proposed and patented by Fessenden (1920). In experimenting with a marine oscillator for generation of acoustic (sound) waves, he noted that the waves were attenuated severely when an automobile air-inflated innertube was placed near the oscillator. Apparently, he confirmed this observation by bubbling air through water in the vicinity of a sound source. In his patent, he proposed that air-bubble streams be used to shield an oscillator (used for sound generation and reception), mounted in the oil tank of a destroyer (Figure 1), from sound waves and also to shield the

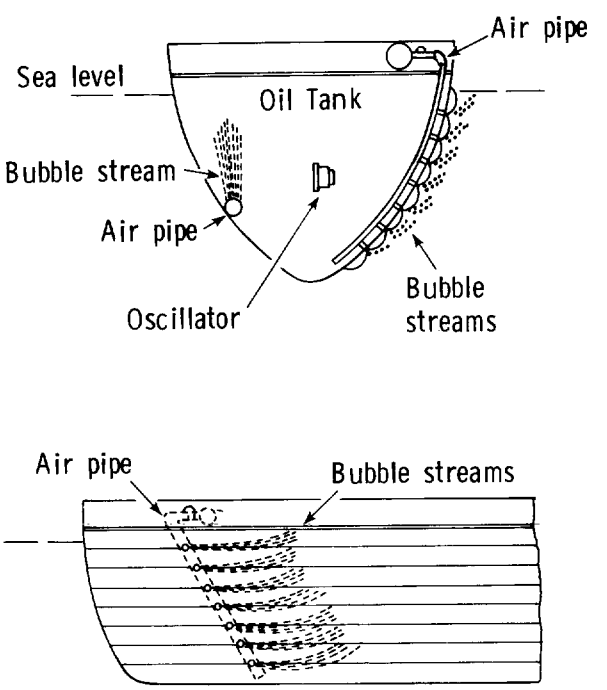


FIG. 1. Vertical cross-sectional views of a destroyer showing how air-bubble streams may be used to shield an oscillator, mounted in the destroyer oil tank, from acoustic waves and also to shield the destroyer from explosive shock waves. (From Fessenden, 1920.)

Manuscript received by the Editor February 23, 1981; revised manuscript received August 6, 1981.
*Amoco Production Company, P.O. Box 591, Tulsa, OK 74102.

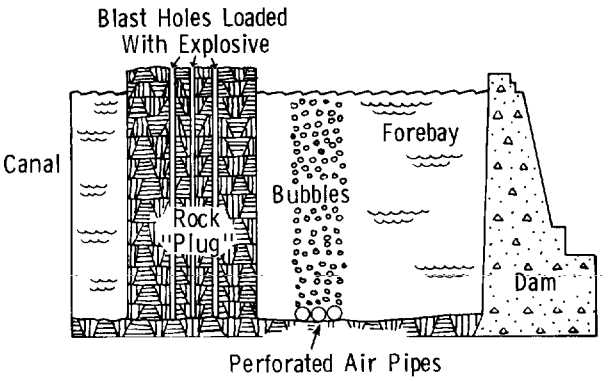


FIG. 2. Cross-section view of the rock barrier ("plug"), forebay, and dam showing air-bubble curtains used to reduce pressure of the explosive shock wave created by blasting of the barrier. (From La Prairie, 1955.)

destroyer from explosive shock waves. As shown in Figure 1, air would issue from the pipe within the oil tank on the port side when it is desired to block sound waves arriving from that direction. Air-bubble streams would be generated outside the destroyer hull as indicated to attenuate explosive shock waves or to block sound waves arriving from that direction. The air streams also would be used to block sound waves from the oscillator in the desired direction.

The effect of air bubbles in water on acoustic wave propagation was studied extensively during World War II. The studies were a small part of an overall effort to utilize underwater sound in antisubmarine and prosubmarine warfare. Most of the information on underwater sound obtained during World War II resulted from a research program organized by the National Defense Research Committee (NDRC) and performed by various U. S. Navy laboratories. Since then, the NDRC technical reports describing this research have been compiled and published in a four-part volume, entitled *Physics of Sound in the Sea*, by the Research Analysis Group of the National Research Council's Committee on Undersea Warfare. Results pertinent to this study are in Part IV of that volume, which is entitled *Acoustic Properties of Wakes*. Since World War II, research has progressed less feverishly in government and university laboratories.

Air-bubble curtains in water currently are used to prevent damage of submerged structures by explosive shock waves as originally conceived by Fessenden (1920). Perhaps the first practical application of this was suggested by La Prairie (1955) as described in the *Compressed Air Magazine* (1954). During the construction of a hydroelectric power facility in Ontario, it was necessary to remove by explosives a rock barrier or "plug" between a canal and the forebay of a dam housing hydroelectric generators (Figure 2). Normally, this would have been done by stopping the generators and draining the forebay before the blasting operation. Alternatively, La Prairie suggested that air curtains be introduced in the forebay between the rock barrier and dam to cushion the shock wave from the blast. Preliminary tests were conducted in a water tank using six parallel perforated air pipes on the tank bottom. Pressures of sound waves from blasting caps at one end were recorded by hydrophones at the other end. Parameters varied were the air flow rate, diameter and spacing

**LIST OF SYMBOLS**

$a, b, d, e$ = Constants in approximate equations for velocity and attenuation [equations (14) and (15)]
$c_0$ = Acoustic wave velocity in water (ft/sec)
$c_g$ = Acoustic wave velocity in air (ft/sec)
$c$ = Acoustic wave velocity in air-water mixture (ft/sec)
$d_w$ = Water depth (ft)
$f$ = Frequency (Hz)
$f_r$ = Resonant frequency (Hz)
$f_* = f/f_r$ Frequency normalized to resonant frequency
$\ell_1$ = Width of air curtain (ft)
$\ell_2$ = Width of bubble-free corridor (ft)
$r$ = Bubble radius (ft)
$s$ = Fractional air volume
$v$ = Bubble velocity (ft/sec)
$A, B$ = Parameters
$C_p$ = Specific heat of air [Btu/(slug °R)]
$F$ = Air flow rate ($ft^3$/sec)
$K$ = Thermal conductivity of air [Btu/(ft sec °R)]
$L = \ell_1 + \ell_2$ Distance between air curtains (ft)
$P_0$ = Ambient pressure (lbs/$ft^2$)
$R$ = Reflection coefficient
$S$ = Normalized stress
$S_n(t)$ = Recorded signal $n$
$S_n(f)$ = Fourier transform of signal $n$
$A_{i,j}$ = Plane wave amplitude for $j$ air curtains at time index $i$
$A_{n,m}$ = Amplitude of signal reflected $n$ times from the water surface and $m$ times from the water bottom
$P_{i,j}$ = Number of equal time raypaths for $j$ air curtains at time index $i$
$Q_{i,j}$ = Matrix for determination of $P_{i,j}$
$Q^T_{i,j}$ = Transpose of $Q_{i,j}$
$X, Y$ = Parameters
$\alpha$ = Acoustic wave attenuation (dB/ft)
$\beta_0$ = Compressibility of water ($ft^2$/lb)
$\beta_g$ = Compressibility of air ($ft^2$/lb)
$\beta$ = Compressibility of air-water mixture ($ft^2$/lb)
$\gamma$ = Adiabatic exponent
$\delta$ = Damping constant
$\delta_* = \delta f_*^2$
$\eta$ = Coefficient of viscosity (lb sec/$ft^2$)
$\mu$ = Polytropic factor
$\rho_0$ = Density of water (lb/$ft^3$)
$\rho_g$ = Density of air (lb/$ft^3$)
$\rho$ = Density of air-water mixture (lb/$ft^3$)
$\sigma$ = Cross-sectional area of air curtain ($ft^2$)
$\tau$ = Time

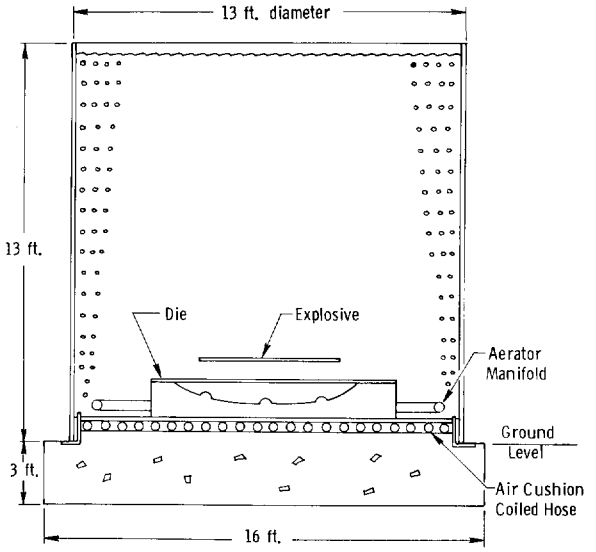


FIG. 3. Cross-section of a cylindrical water-filled explosive forming tank with a bottom air cushion and a circumferential air-bubble curtain to attenuate the explosive shock wave. (From Pipher et al, 1960.)

of the holes in each pipe, pipe spacing, and number of pipes. La Prairie concluded that the sound wave pressure could be reduced approximately 90 percent by an air curtain of *reasonable* density. Subsequently, three perforated air pipes were positioned in the forebay of the dam (Figure 2) and were supplied air at a rate of 3750 $ft^3$/minute and a pressure of 90 psi during blasting of the rock barrier. Pressures measured at the dam proved to be well below the damaging level. It was estimated that savings realized by continuous operation of the generators (no loss of electric power) and by elimination of the need to drain the forebay amounted to about $1 million. Since this operation, air curtains have been used routinely to protect underwater structures from damage by underwater explosions, guidelines for which are given in Langefors and Kihlström (1967).

A similar application of air curtains is in explosive metalworking operations. These involve forming of metals by explosives and often are conducted in a large water-filled cylindrical tank, as shown in Figure 3, to protect the surroundings from damage. In addition to thick walls and various means of cushioning the bottom, an air bubble screen is created inside the tank around its circumference (Figure 3). Pipher, et al (1960) experimented to determine the circumferential stress created in the wall of a cylindrical water-filled tank, 24 inches in diameter and 35 inches high, by an explosive charge positioned on the tank axis 18 inches from the bottom. The charge consisted of a no. 6 blasting cap and 20 grains of PETN Primacord. Strain gauges were mounted on the outside of the tank at the height of the charge. Air was supplied to a 2-inch diameter perforated pipe at the tank bottom around the circumference. Holes were 0.07 inch in diameter and spaced 0.50 inch apart. The stress was measured for different air flow rates. The data are plotted in Figure 4 where the stress is in decibels relative to the stress measured without the circumferential air bubble curtain (0 $ft^3$/minute). The stress appears to decrease exponentially with increasing air flow at a rate of about 1.14 dB/$ft^3$/minute.

A possible application of air-bubble curtains in water to marine seismic exploration was demonstrated in physical model experiments by Sarrafian (1956). Briefly, he generated and recorded sound waves in a laboratory steel water tank to confirm the presence and nature of multiple reflections between the top water-air interface and the tank bottom. In investigating methods for attenuating multiple reflections, he placed a plastic box in the water tank midway between the hydrophone (H) and spark-gap source (S) as shown in Figure 5a. The open top of the box was a few millimeters below the surface, and the acoustic impedance of the box sides was approximately equal to that of water. He noted no change in the received signal (Figure 5b) after the box was in place and full of water. Then an effervescent powder was placed in the box and another signal was recorded (Figure 5c). It is obvious that the bubbles generated in the box effectively attenuated reflections. Resonant frequencies of multiple reflections in the water tank may be obtained from (Backus, 1959),

$$f_n = \frac{2n - 1}{4d_w} c_0,$$

where $f_n$ is the resonant frequency for mode $n$, $c_0 = 1.46 \cdot 10^5$ cm/sec is sound velocity in water, and $d_w = 8$ cm is the water depth. The time interval of the first half-cycle of the direct wave recorded by the hydrophone is approximately 10 μsec, corresponding to a frequency of 50 kHz. This frequency is nearly equal to that of the sixth mode ($f_6 = 50.19$ kHz) at which the wavelength is 2.9 cm. The width and depth of the box expressed in wavelengths (for $n = 6$) is approximately 1.7 and 1.0, respectively; thus, the attenuation per wavelength is appreciable.

Since none of the previously published investigations included

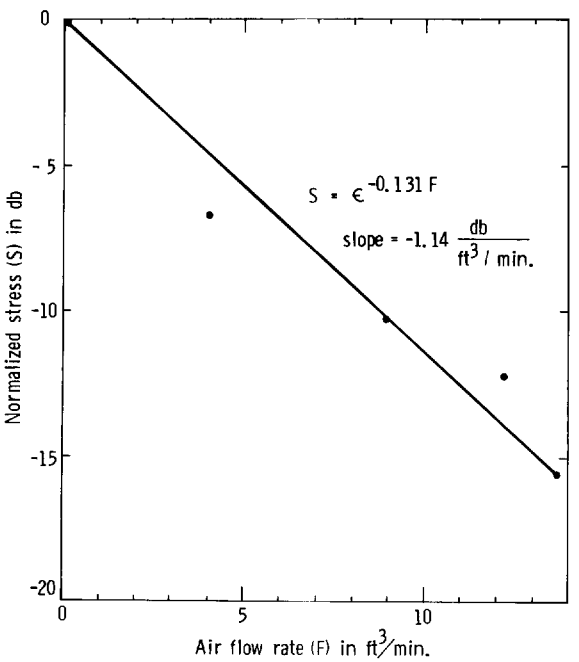


FIG. 4. Circumferential stress versus air flow rate for explosions in a cylindrical water-filled tank with a circumferential air-bubble curtain. (Adapted from Pipher et al, 1960.)

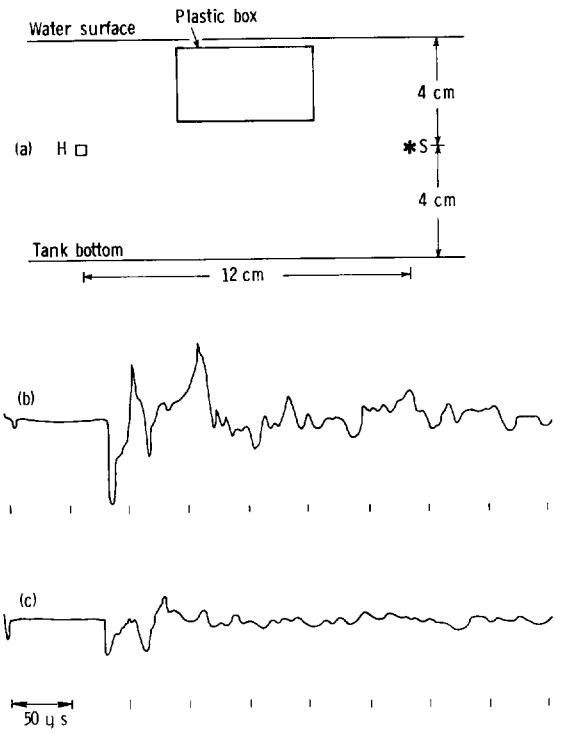


FIG. 5. Experiment for determination of acoustic wave attenuation in a water tank by bubbles from an effervescent powder placed in a plastic box. (a) Cross-sectional view of water tank showing location of hydrophone (H) and source (S). (b) Signal recorded without bubbles. (c) Signal recorded with bubbles. (From Sarrafain, 1956.)

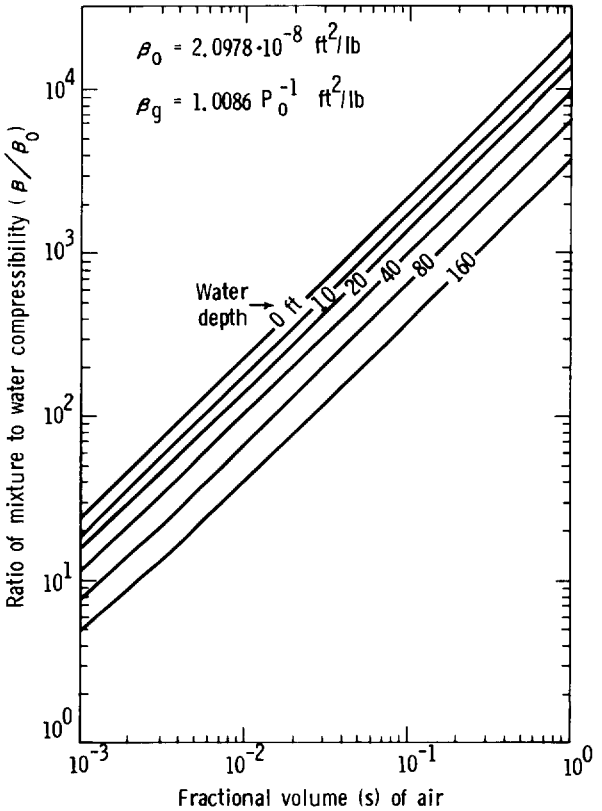


FIG. 6. Ratio of compressibility β of air-bubble/water mixture to compressibility $\beta_0$ of bubble-free water versus fractional volume $s$ of air in the mixture, for ambient pressures $P_0$ corresponding to water depths shown.

marine seismic source signals, a field experiment was conducted to determine the attenuation by air-bubble curtains in water of sound from a marine seismic source, namely, a water gun. The latter was chosen because of its essentially bubble-free signature. Bubble oscillations, of course, would complicate signal analysis substantially. As noted previously, this field experiment is the subject of Domenico (1982).

## THEORY

Published theory and experimental verification concerning sound attenuation by bubbles in a liquid is extensive and will not be summarized here. Such papers directly or obliquely related to this study are listed under References for General Reading. Motivation for much of this previous effort was the observation that wakes of ships, mixtures of air bubbles and water, often severely attenuate sound waves. This phenomenon, of course, was of prime concern during World War II when the initial studies were conducted.

### General

As noted previously, air bubbles in water greatly increase the compressibility and thereby increase the attenuation and reduce the velocity several fold from corresponding values for bubble-free water. Air compressibility $\beta_g$ at a temperature of 47°F is closely approximated by (Hilsenrath, 1972)

$$\beta_g = 1.0086\ P_0^{-1}\ \text{ft}^2/\text{lb}, \tag{1}$$

where $P_0$ is the ambient pressure in lb/ft². Water compressibility and density at ambient pressures from 1 to 6 atm, corresponding to water depths from 0 to 160 ft, varies negligibly. Water compressibility $\beta_0$ used in this study is $2.0978 \cdot 10^{-8}$ ft²/lb, which corresponds to a water density $\rho_0$ of 2.01 slugs/ft³ (1.035 g/cm³) and a sound velocity in water $c_0$ of 4870 ft/sec which are believed appropriate values for this study.[1] The compressibility β of an air-bubble/water mixture is the weighted-by-volume average of the water and air compressibilities,

$$\beta = (1 - s)\beta_0 + s\beta_g\ \text{ft}^2/\text{lb}, \tag{2}$$

where $s$ is the fractional volume of air in the mixture. The ratio $\beta/\beta_0$ is plotted versus $s$ in Figure 6 for ambient pressures corresponding to water depths from 0 to 160 ft. Similar to compressibility, the density ρ of the mixture is given by the weighted-by-volume average of water density $\rho_0$ and air density $\rho_g$,

$$\rho = (1 - s)\rho_0 + s\rho_g\ \text{slugs/ft}^3. \tag{3}$$

Air density $\rho_g$ at a temperature of 47°F is closely approximated by (Hilsenrath, 1972)

$$\rho_g = 1.0714 \cdot 10^{-6} P_0^{1.0086}\ \text{slugs/ft}^3, \tag{4}$$

where $P_0$ is in lbs/ft².

[1] One slug = 32.15 lbs.

At sound frequencies well below the resonant frequencies of the bubbles, sound velocity $c$ in the air-bubble/water mixture is given by

$$c = \sqrt{\frac{1}{\beta\rho}} \text{ ft/sec}, \tag{5}$$

where $\beta$ and $\rho$ are given by equations (2) and (3), respectively. Similar to the graph in Figure 6, the graph in Figure 7 shows the ratio $c/c_0$, where $c_0$ is sound velocity in bubble-free water,

$$c_0 = \sqrt{\frac{1}{\beta_0\rho_0}} \text{ ft/sec}, \tag{6}$$

versus the air fractional volume $s$ for ambient pressures corresponding to the indicated water depths. Equation (5) is equivalent to Wood's equation (Wood, 1949) who first showed the peculiar nonlinear variation of sound velocity in an air-water mixture as the fractional air volume varies. In a mixture containing only one part air to 1000 parts mixture ($s = 0.001$), the velocity is reduced from 4870 ft/sec in bubble-free water to 1000 ft/sec at 0-ft depth and to 2210 ft/sec at 160-ft depth.

Velocity is at a minimum near $s = 0.5$ where it is well below sound velocity in air, being 64.6 ft/sec at 0-ft depth and 156.2 ft/sec at 160-ft depth.

As sound frequencies increase and approach bubble resonant frequencies, equation (5) becomes increasingly inaccurate. Silberman (1957) summarized previous theoretical derivations by Spitzer (1943) to obtain general equations for velocity and attenuation which appear to account for bubble resonance effects accurately. His equation for velocity is

$$\left(\frac{c_0}{c}\right)^2 = \frac{1 + AX}{2}\left\{1 \pm \left[1 + \left(\frac{AY}{1 + AX}\right)^2\right]^{1/2}\right\}, \tag{7}$$

where

$$A = \frac{\rho c_0^2}{\gamma p_0}$$

in which $\gamma$ is the adiabatic exponent, and the parameters $X$ and $Y$ are

$$X = \frac{s(1 - f_*^2)}{(1 - f_*^2)^2 + \delta_*^2}, \tag{8}$$

and

$$Y = \frac{s\delta_*}{(1 - f_*^2)^2 + \delta_*^2}. \tag{9}$$

In equations (8) and (9), $f_* = f/f_r$, where $f$ is frequency in Hz, $f_r$ is the bubble resonant frequency, and $\delta_* = \delta f_*^2$, where $\delta$ is the bubble damping constant. The attenuation $\alpha$ is given by

$$\alpha = \frac{c}{c_0^2}\pi f A Y \quad \text{nepers/ft}. \tag{10}$$

The resonant frequency $f_r$ and damping constant $\delta_*$ are given by

$$f_r = \frac{1}{2\pi r}\left(\frac{3\mu\gamma P_0}{\rho}\right)^{1/2} \text{ Hz}, \tag{11}$$

and

$$\delta_* = \mu^2 B\left[1 - \frac{2B}{3(\gamma - 1)}\right] + f_*^3\left(\frac{3\mu}{A}\right) + \frac{8\pi\eta f}{3\gamma P_0}, \tag{12}$$

in which $r$ is the bubble radius, $\mu$ is the polytropic factor $(1/\gamma \le \mu \le 1)$, $\eta$ is the coefficient of water viscosity, and $B$ is given by

$$B = \frac{3}{2}\frac{\gamma - 1}{r}\left[\frac{K}{\pi\rho_g C_p f}\right]^{1/2} \tag{13}$$

where $K$ is the thermal conductivity of air and $C_p$ is the specific heat of air at constant pressure. The polytropic factor $\mu$ is given by $\mu \approx 1/(1 + \beta)$. The three terms on the right side of equation (12) describing the damping constant $\delta_*$ express, in order, the contribution of (1) heat conduction from the pulsating bubbles, (2) sound reradiation by the bubbles, and (3) viscous damping by the water in the immediate vicinity of each bubble. The first term is valid only when $B < 0.6(\gamma - 1)$. The relative contributions of each term will be shown below.

Equations (7) and (10) apply only to a homogeneous mixture containing spherical bubbles of equal radius $r$ greater than 0.0005 ft and much less than the smallest sound wavelength. Also, the fractional air volume $s$ must be less than 0.03. Equation (7) reduces to Wood's equation [equation (5)] at $f = 0$ and to $c = c_0$ at $f = \infty$. The attenuation $\alpha$ given by equation (10) becomes zero at $f = 0$.

Silberman (1957) verified equations (7) and (10) by laboratory measurements of sound velocity and attenuation in a cylinder containing water, at the bottom of which bubbles were injected. Well below the bubble resonant frequency, continuous monofrequency sound signals were generated creating standing waves between the bottom and top of the column, the latter being open to the atmosphere. Velocity was obtained by locating pressure nodes and antinodes, and the attenuation was obtained by mea-

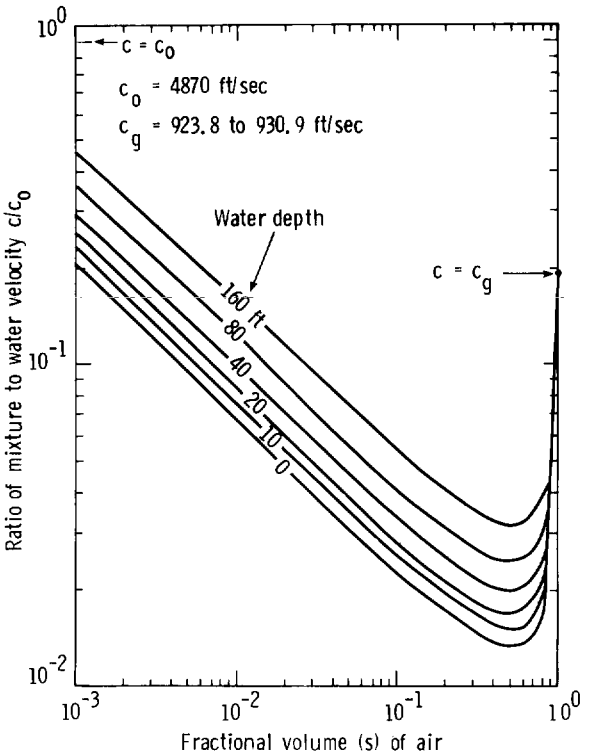


FIG. 7. Ratio of velocity $c$ in an air-bubble/water mixture to velocity $c_0$ in a bubble-free water versus fractional volume $s$ of air in the mixture, for ambient pressures $P_0$ corresponding to water depths shown.

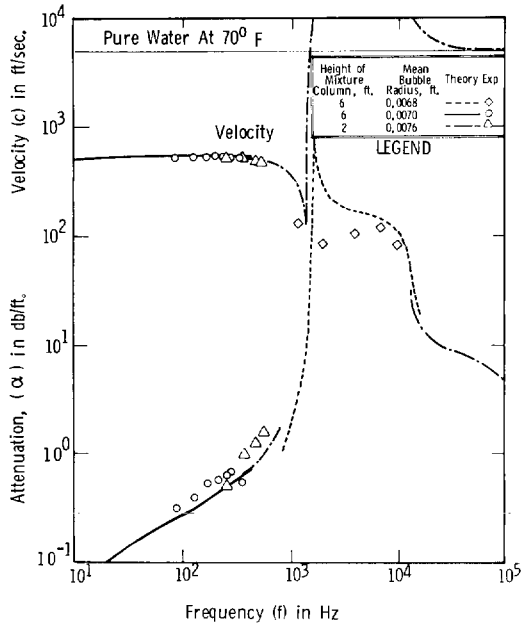


FIG. 8. Theoretical and measured velocities and attenuations versus frequency (from Silberman, 1957).

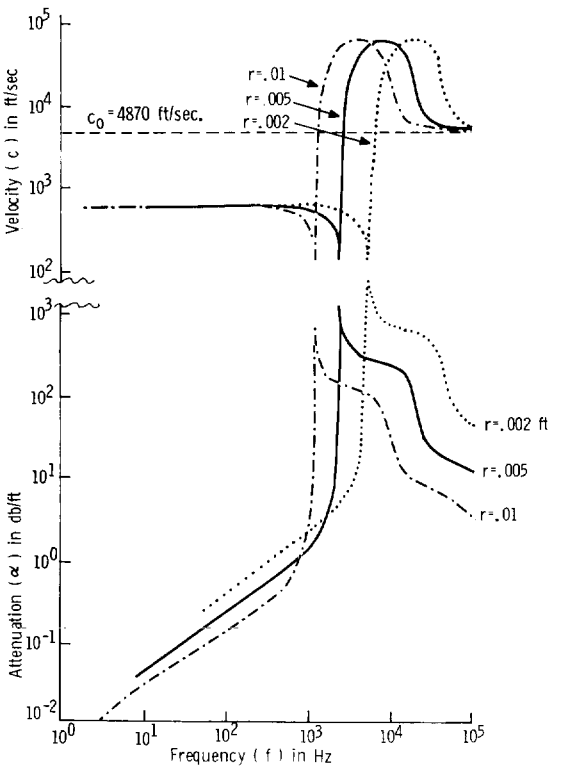


FIG. 9. Theoretical velocity $c$ and attenuation $\alpha$ versus frequency curves derived from equations (7) and (10), respectively, for a fractional air volume $s$ of 0.006 and for each of three bubble radii $r$, specifically, 0.002, 0.005, and 0.01 ft. Ambient pressure $P_0$ corresponds to a water depth of 12 ft.

**Table 1. Values of parameters believed to be representative of test site physical characteristics.**

| Parameter | Value | Units |
|---|---|---|
| Temperature | 47 (507) | °F (°R) |
| Water salinity | 35,000 | mg/liter |
| Water density ($\rho_0$) | 1.035 (2.01) | g/cm$^3$ (slugs/ft$^3$) |
| Air density ($\rho_g$) | $1.73 \cdot 10^{-3}$ ($3.36 \cdot 10^{-3}$)* | g/cm$^3$ (slugs/ft$^3$) |
| Water velocity ($c_0$) | 4870 | ft/sec |
| Specific heat of air ($C_p$) | 10.83 | Btu/(slug °R) |
| Coefficient of viscosity ($\eta$) | $2.902 \cdot 10^{-5}$ | lb sec/ft$^2$ |
| Ambient pressure ($P_0$) | 20.08 (2892.3)* | psi (lb/ft$^2$) |
| Adiabatic exponent ($\gamma$) | 1.40 | — |
| Thermal conductivity of air ($K$) | $3.96 \cdot 10^{-6}$ | Btu/(ft sec °R) |

*Corresponds to a water depth of 12 ft.

suring the relative amplitudes of the nodes and antinodes. At frequencies approaching the bubble resonant frequency, attenuation was too high for generation of standing waves. Attenuation was determined by making pressure amplitude measurements at small depth intervals near the sound source. Velocity could not be determined at these frequencies. The average fractional volume of air was determined by comparing the weight of the column of the air-bubble/water mixture to the weight of a water column of equal dimensions. (The fractional volume, of course, varied vertically slightly since the bubbles expanded as they rose in the column.)

In a sequence of seven experiments, frequency was varied from 100 Hz to 10 kHz, bubble radius was varied from about $6 \cdot 10^{-4}$ to $10^{-2}$ ft, and fractional air volume was varied from about $3.5 \cdot 10^{-3}$ to $10^{-2}$. Measured velocities and attenuations were plotted versus frequency and compared to theoretical curves derived from equations (7) and (10) as shown in Figure 8. The measured values actually are from three separate measurement sets between which the mean bubble radius varied slightly and column height was changed as shown. The measured air fractional volume was 0.0053 ft. The theoretical curves were derived for each radius and column height. Attenuation is in dB/ft which requires that computations from equation (10) be multiplied by 20 log $e$. The theoretical velocity curve shows that below the resonant frequency ($f < f_r$) the velocity is nearly constant, well below the velocity in bubble-free water and also below velocity in air (~1100 ft/sec). Near $f_r$ the velocity decreases to a sharp minimum, thereafter rising to a broad maximum (incompletely shown) well above velocity in water and then decreasing to the latter velocity. Velocity measurements at frequencies below $f_r$ agree well with the theoretical curve. Theoretical attenuation curves demonstrate that below $f_r$ the attenuation increases rapidly with increasing frequency from less than $10^{-1}$ dB/ft at 10 Hz to almost $10^3$ dB/ft at $f_r$. Thereafter, the attenuation decreases at a varying rate, remaining above 100 dB/ft to a frequency of about $10^4$ Hz. Measured attenuations agree satisfactorily with the theoretical curves, demonstrating the large increase near $f_r$.

## Test site parameters

The field experiment, described in Domenico (1982), consisted of placing 13 perforated air pipes in a parallel configuration

at the bottom of a 25-ft deep test pond. Air-bubble curtains issued from the pipes at different air pressures. A marine water gun, the sound source, was suspended at mid-depth off one side at right angles to the air curtains. Off the opposite end three hydrophones, also suspended at mid-depth, were spaced along a line at right angles to the air curtains. Signals from the water gun were recorded in digital form (0.25-msec sample interval) as the air curtains were activated in sequence. Prior to this experiment, theoretical values were computed from equations (7) and (10) to serve as background information for the subsequent field experiment. Values and units of the parameters used, which are believed to be representative of test site physical characteristics, are listed in Table 1. Theoretical velocity and attenuation versus frequency curves were derived (Figure 9) for a fractional air volume $s$ of 0.006 and for each of three bubble radii $r$, specifically, 0.002, 0.005, and 0.01 ft. The ambient pressure $P_0$ corresponds to a water depth of 12 ft. Unfortunately, it was not possible to observe bubble size in the experiment. The holes drilled in the air pipes were 3/64 inches in diameter or 0.002 ft in radius. The latter is the minimum radius of the bubble and the maximum, according to Lamb (1932), is 6.48 times the hole radius or, in this experiment, approximately 0.01 ft. Thus, the radii used range from the minimum to maximum possible bubble radius. Of course, the bubbles do expand slightly as they rise to the surface.

The theoretical curves in Figure 9 show the velocity $c$ in the mixture is nearly constant (approximately 600 ft/sec) and is insensitive to bubble radius to a frequency of about 300 Hz. As frequency increases, velocities decrease to minima at bubble resonant frequencies, increase abruptly to broad maxima, and then decrease to the velocity $c_0$ in air-free water. Below bubble resonances, the attenuation increases at a rate proportional to approximately the 0.7 power of frequency and also increases with decreasing bubble radius. The curves cross before peak values at bubble resonances, attaining maximum values of 573 dB/ft for $r$ = 0.01 ft to 2270 dB/ft for $r$ = 0.002 ft. Above the resonant frequency the curves remain separated, the attenuation again increasing with decreasing bubble radius.

A plot of resonant frequency $f_r$ [derived from equation (11)] versus bubble radius $r$ is shown in Figure 10. The resonant frequency is inversely proportional to bubble radius, decreasing two orders of magnitude as bubble radius increases from 0.001 to 0.1 ft (approximately 12.5 kHz to 125 Hz). Density $\rho$ of the air-bubble/water mixture over the range of fractional air volumes $s$ considered here affects the resonant frequency only slightly as indicated by the near coincidence of the curves for $s$ = 0.001 and $s$ = 0.1 in Figure 10. The frequency difference for these extreme values is about 5.3 percent.

The effect of fractional air volume $s$ on velocity and attenuation was investigated by varying $s$ from 0.001 to 0.1 (some-

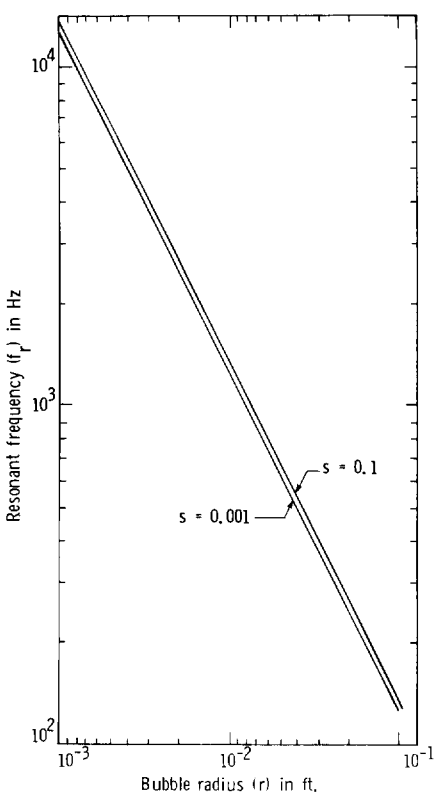


FIG. 10. Resonant frequency $f_r$ versus bubble radius $r$ for fractional air volumes of 0.001 and 0.1.

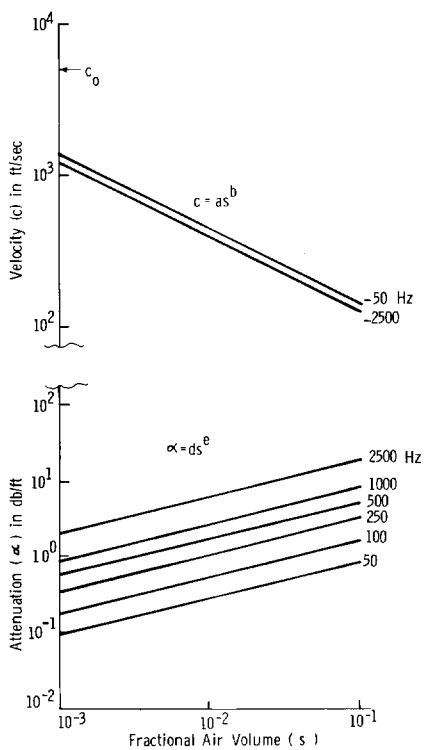


FIG. 11. Theoretical velocity $c$ and attenuation $\alpha$ versus fractional air volume $s$ derived from equations (7) and (10), respectively, for a bubble radius $r$ of 0.002 ft and for frequencies from 50 to 2500 Hz. Ambient pressure $P_0$ corresponds to a water depth of 12 ft.

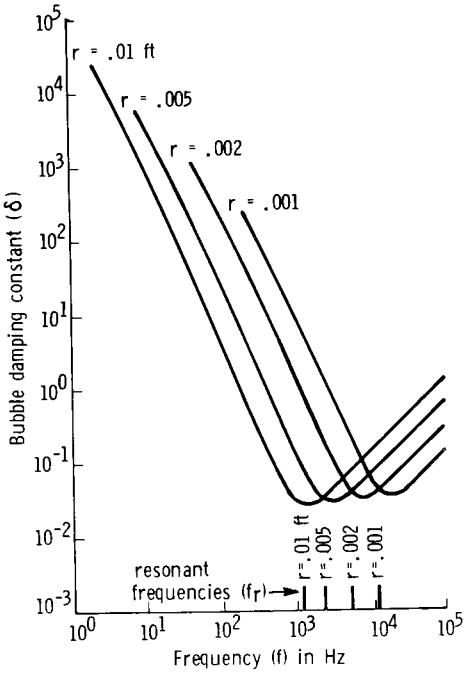


FIG. 12. Bubble damping constant δ versus frequency $f$ derived from equation (12) for a fractional air volume $s$ of 0.006 and for bubble radii $r$ shown. Bubble resonant frequencies $f_r$ are indicated. Ambient pressure $P_0$ corresponds to a water depth of 12 ft.

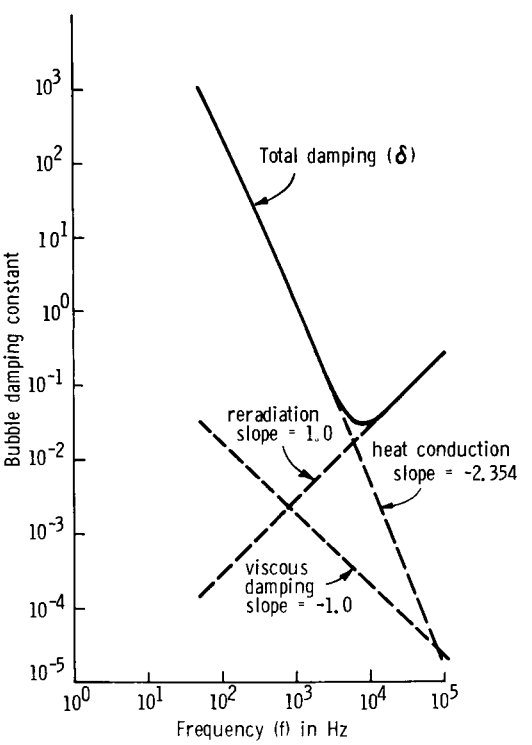


FIG. 13. Total damping δ and each of three terms comprising total damping [equation (12)] versus frequency $f$. The terms express, respectively, the contribution of heat conduction, sound reradiation, and viscous damping. The total damping curve is identical to the curve in Figure 12 for a bubble radius $r$ of 0.002 ft.

what exceeding the theoretical limit of 0.03) for a constant bubble radius of 0.002 ft and for constant frequencies from 50 to 2500 Hz (Figure 11). As shown in Figure 11, the attenuation increases and the velocity decreases exponentially with increasing air volume, the velocity being much less sensitive to frequency. Over the indicated range of fractional air volume and frequency the curves are approximated closely by the functions

$$c = as^b \text{ ft/sec} \tag{14}$$

for velocity and

$$\alpha = ds^e \text{ dB/ft} \tag{15}$$

for attenuation. The constants $a$, $b$, $d$, and $e$ are listed in Table 2. In addition to the constants for the frequencies shown in Figure 11, constants $a$ and $b$ for velocity at 0 Hz are given, which is equivalent to Wood's velocity equation [equation (5)]. The velocity and attenuation are closely proportional to the square root of the air volume.

The final theoretical investigation was to determine the effect of the three terms in equation (12),

$$\delta_* = \mu^2 B\left[1 - \frac{2B}{3(\gamma - 1)}\right] + f_*^3\left(\frac{3\mu}{A}\right) + \frac{8\pi\eta f}{3\gamma\rho_0}, \tag{12}$$

on the bubble damping $\delta = \delta_*/f_*^2$. As mentioned previously, the three terms express, in order, the contribution of (1) heat conduction from the pulsating bubbles, (2) sound reradiation by the bubbles, and (3) viscous damping by the water in the immediate vicinity of each bubble. First the damping constant was computed, using parameters given in Table 1, as a function of frequency for a fractional air volume of 0.006 and for each of four bubble radii, specifically, 0.001, 0.002, 0.005, and 0.01 ft (Figure 12). As shown in Figure 12, the damping constant for each bubble radius decreases with increasing frequency to a minimum somewhat above the resonant frequency, the departure increasing as the bubble radius decreases. At frequencies below the minima, the damping constant increases with decreasing bubble radius, whereas the opposite occurs at the frequencies above. Next, the three terms in equation (12) were evaluated separately for a bubble radius of 0.002 ft and fractional air volume of 0.006, corresponding to one curve in Figure 12. Each term, as well as the sum of the terms or the damping constant, is plotted versus frequency in Figure 13. It is apparent that heat conduction is dominant below and reradiation is dominant above the frequency at the minimum value. Viscous damping is not significant.

## CONCLUSIONS

The effect of gaseous bubbles in a fluid on acoustic wave velocity and attenuation has been examined extensively in the past, both theoretically and experimentally. Air bubbles in water increase the compressibility several orders of magnitude above that in bubble-free water and thereby greatly reduce the velocity and increase the attenuation of acoustic waves. Practical applications include prevention of damage by explosive shock waves to submerged structures and to water-filled tanks in explosive metal working operations through the proper placement of air-bubble curtains which absorb the wave energy.

Laboratory experiments, which generally have confirmed theoretical velocity and attenuation functions, demonstrate that these quantities are dependent principally upon frequency, bubble size, and fractional volume of air. Below the bubble resonant frequency the velocity is nearly frequency-independent

**Table 2. Values of constants in equations (14) and (15) which are approximations to curves in Figure 11.**

| Frequency ($f$) in Hz | $c = as^b$ | | $\alpha = ds^e$ | |
|---|---|---|---|---|
| | $a$ | $b$ | $d$ | $e$ |
| 0 | 41.89 | −0.482 | | |
| 50 | 46.07 | −0.491 | 2.88 | 0.509 |
| 100 | | | 5.44 | 0.509 |
| 250 | | | 10.98 | 0.509 |
| 500 | | | 17.61 | 0.508 |
| 1000 | | | 27.91 | 0.507 |
| 2500 | 41.92 | −0.490 | 61.25 | 0.499 |

and well below the velocity in bubble-free water. Near the resonant frequency the velocity decreases to a sharp minimum and then, as frequency increases beyond the resonant frequency, increases abruptly to a broad maximum well above velocity in water. Finally, as frequency increases further, the velocity decreases to that in bubble-free water. Initially, attenuation increases gradually with increasing frequency and then rapidly as the resonant frequency is approached, attaining a maximum value several orders of magnitude above that at low frequency. Beyond resonance, attenuation decreases gradually. The resonant frequency is inversely proportional to bubble radius.

Theoretical calculations preceding a field experiment, described in Domenico (1982) and based on physical parameters at the test site, indicated the variation in velocity and attenuation to be expected within the anticipated range of frequency, bubble size, and fractional air volume. These demonstrated that velocity is insensitive to frequency below approximately 300 Hz and to bubble radius which was varied from 0.01 to 0.002 ft, corresponding to resonant frequencies of 1240 to 6204 Hz, respectively. Below bubble resonance, attenuation increases at a rate proportional to approximately the 0.7 power of frequency and decreases with increase in bubble radius. Attenuation ranges from values in the vicinity of 0.01 dB/ft at 10 Hz to values of 573 and 2270 dB/ft at the resonant frequencies for bubble radii of 0.01 and 0.002 ft, respectively. For a range of fractional air volume from 0.001 to 0.1, the velocity decreases and the attenuation increases at a rate approximately proportional to the square root of the air volume. Finally, it was determined that attenuation is due essentially to heat conduction from the pulsating bubbles below the resonant frequency and to sound reradiation above the resonant frequency. Viscous damping is not significant.

## ACKNOWLEDGMENTS

The author expresses his appreciation to Prof. E. Silberman, Saint Anthony Falls Hydraulic Lab., for his guidance in application of theory to estimation of acoustic wave velocity and attenuation in an air-bubble/water mixture of known or assumed physical properties. Also, he is indebted to C. Crowe, staff research scientist, Amoco Research Center, for invaluable counseling and referrals to published material, and to his assistant, Jana Burgin, for computations, construction of graphs, and proofreading.

## REFERENCES

Backus, M. M., 1959, Water reverberations—Their nature and elimination: Geophysics, v. 24, p. 233–261.
Compressed Air Magazine, 1954, v. 59, p. 230.
Domenico, S. N., 1982, Acoustic wave propagation in air bubble curtains in water—Part II: Field experiment: Geophysics, v. 47, this issue, p. 354–375.
Fessenden, R. A., 1920, Method and apparatus for sound insulation: U.S. Patent no. 1,348,828.
Hilsenrath, J., 1972, Thermodynamic properties of gases, *in* American Institute of Physics Handbook: New York, McGraw-Hill, p. 4–165.
Lamb, H., 1932, Hydrodynamics, 6th ed.: Cambridge, The University Press.
Langefors, U., and Kihlström, B., 1967, The modern technique of rock blasting: New York, John Wiley and Sons.
La Prairie, A. J. C., 1955, Method of blasting: U.S. Patent no. 2,699,117.
Pipher, F. C., Rardin, G. N., and Richter, W. L., 1960, High energy rate metal forming: Final technical engineering report, Lockheed Aircraft Corp., Burbank, CA.
Sarrafian, G. P., 1956, A marine seismic model: Geophysics, v. 21, p. 320–336.
Silberman, E., 1957, Sound velocity and attenuation in bubbly mixtures measured in standing wave tubes: J. Acoust. Soc. Am., v. 29, p. 925–933.
Spitzer, L., Jr., 1943, Acoustic properties of gas bubbles in a liquid: OSRD 1705, NDRC 6.1-SR20-918, CUSWR, 70 p.
Wood, A. B., 1949, A textbook of sound: London, G. Bell and Sons, Ltd., p. 361–362.

## REFERENCES FOR GENERAL READING

Anderson, A. L., and Hampton, L. D., 1980, Acoustics of gas-bearing sediments. I. Background and II. Measurements and models: J. Acoust. Soc. Am., v. 67, p. 1865–1903.
Brandt, H., 1960, Factors affecting compressional wave velocity in unconsolidated marine sand sediments: J. Acoust. Soc. Am., v. 32, p. 171.
Busby, J., and Richardson, E. G., 1957, The absorption of sound in sediments: Geophysics, v. 22, p. 821.
Cartensen, E. E., and Foldy, L. L., 1947, Propagation of sound through a liquid containing bubbles: J. Acoust. Soc. Am., v. 19, p. 481.
Davids, N., and Thurston, E. G., 1950, The acoustical impedance of a bubbly mixture and its size distribution function: J. Acoust. Soc. Am., v. 22, p. 20–23.
Devin, C. Jr., 1959, Survey of thermal, radiation, and viscous damping of pulsating air bubbles in water: J. Acoust. Soc. Am., v. 31, p. 1654.
Eller, A. I., 1970, Damping constant of pulsating bubbles: J. Acoust. Soc. Am., v. 47, p. 1469.
Faas, R. W., 1969, Analysis of the relationship between acoustic reflectivity and sediment porosity: Geophysics, v. 34, p. 546.
Fox, F. E., Curley, S. R., and Larson, G. S., 1955, Phase velocity and absorption measurements in water containing air bubbles: J. Acoust. Soc. Am., v. 27, p. 534.
Gibson, F. W., 1970, Measurement of the effects of air bubbles on the speed of sound in water: J. Acoust. Soc. Am., v. 48, p. 1195.
Houghton, G., 1963, Theory of bubble pulsation and cavitation: J. Acoust. Soc. Am., v. 35, p. 1387.
Kinsler, K. E., and Frey, A. R., 1959, Fundamentals of acoustics: New York, John Wiley and Sons.
Laird, D. T., and Kendig, P. M., 1952, Attenuation of sound in water containing air bubbles: J. Acoust. Soc. Am., v. 24, p. 29.
Macpherson, J. D., 1957, Effect of gas bubbles on sound propagation in water: Proc. Phys. Soc., London, B70, p. 85.
Mole, L. A., Hunter, J. L., and Davenport, J. M., 1972, Scattering of sound by air bubbles in water: J. Acoust. Soc. Am., v. 52, p. 837.
Sage, K. A., George, J., and Überall, H., 1979, Multipole resonances in sound scattering from gas bubbles in a liquid: J. Acoust. Soc. Am., v. 65, p. 1413–1422.
Strasberg, M., 1953, The pulsation frequency of nonspherical gas bubbles in liquids: J. Acoust. Soc. Am., v. 25, p. 536–537.
van Wijngaarden, L., 1972, One-dimensional flow of liquids containing small gas bubbles: Annual Rev. Fluid Mechanics, v. 4, p. 369–396, Twente Inst. Tech., Enschede, The Netherlands.

GEOPHYSICS, VOL. 47, NO. 3 (MARCH 1982); P. 354–375, 28 FIGS., 5 TABLES.



# Acoustic wave propagation in air-bubble curtains in water—Part II: Field experiment

S. N. Domenico*


## ABSTRACT

A field experiment consisted of hydrophone recordings in a pond, 25 ft deep, of signals transmitted through air-bubble curtains from a water gun source. The air curtains issued from one to 13 pipes (20 ft long and spaced at 1.67 ft intervals). Air pressures used in the pipes were 15, 25, and 50 psi. Length and complexity of the signals indicate that reverberations occurred to an increasing extent as the number of consecutive air curtains was increased. Analysis of the first pulse in the recorded signals, after approximate removal of hydrophone and recorder response, indicates that the reverberations occur principally in the bubble-free corridors between air curtains. This pulse broadens and its peak amplitude is delayed linearly as the number of successive air curtains is increased. The peak amplitude is decreased substantially by the first air curtain and thereafter remains between 0.1 and 0.2 of the amplitude without air curtains. The time delay increases measurably, whereas the amplitude appears insensitive to an increase in air pressure.

Width of the bubble-free corridor, velocity in the air curtains, and reflection coefficient at the air curtain/corridor interface were determined for each of the three air pressures from signal onset times and delay time of the first pulse peak amplitude. The corridor width was approximately three times the air curtain width and did not appear to vary with air pressure. Traveltime in the air curtain, however, increased with air pressure and was from three to four times the traveltime in the corridor. Reflection coefficients ranged from about 0.75 at 15 psi to 0.82 at 50 psi. These data were used to predict, successfully, times of multiple reflections between the outer interfaces of the outermost air curtains.

Plane-wave synthetic signals, based on absorptionless models simulating the air curtain configurations and velocities, correspond satisfactorily to recorded signals for the successive-pipe sequence. As for the recorded signals, peak amplitude of the first pulse is decreased substantially by a single air curtain and not appreciably more by additional air curtains. Recorded-signal amplitudes, however, exceed synthetic-signal amplitudes, possibly due to inadequacy of the plane-wave models and to backscattered signals within the pond.

The dominant reverberations prevented meaningful measurements of the frequency-dependent absorption in the air curtains. Theoretical absorption values were obtained after synthetically eliminating the bubble-free corridors by expansion of the air curtains. Absorption as a function of air curtain width was determined for each of the three air pressures and for the extremes of possible bubble radii (0.002 to 0.014 ft). Similar to reduction of the first pulse peak amplitude on recorded signals, amplitude of synthetic signals is decreased substantially by the air curtain from a single pipe and at a much lower rate as the air curtain width increases. Frequency-dependent absorption for the smaller bubble radius (0.002 ft) is substantially greater and increases with air curtain width at a greater rate.


## INTRODUCTION

Following the review of theoretical and experimental efforts by other investigators and determination of theoretical functions, which should be applicable to a test site at which a field experiment was planned [both described in Domenico (1982, this issue)], this experiment was conducted. Here a description and results of the experiment are given.[1]

## EXPERIMENT DESCRIPTION

The field experiment was performed in a pond near Friendswood, a village approximately 5 mi southeast of Houston, Texas. The pond was designed specifically for testing of marine equipment. The pond (Figure 1) is a square, 200 by 200 ft, the bottom sloping downward uniformly to a depth of 25 ft at the center. A pier extending from one side provides access to the pond's center.

[1] A list of the symbols used is included in Part I, p. 346, this issue.

Manuscript received by the Editor February 23, 1981; revised manuscript received August 6, 1981.
*Amoco Production Company, P.O. Box 591, Tulsa, OK 74102.

Figure 2 is a plan and section view of the arrangement of perforated air pipes, water gun, and hydrophones. Thirteen plastic pipes, 1-inch ID, each 20 ft in length, were mounted in a 20 by 20 ft frame at a spacing of 1.67 ft (20 inches). Holes, 3/64 inch in diameter, were drilled at 4-inch intervals along each pipe (60 holes per pipe). The pipe frame was suspended from buoys at a depth of 24 ft, a few inches above the bottom. A water gun was suspended from a spacing bar, supported by buoys, 12 ft deep and 3 ft from the pipe frame side.

Four hydrophones of the same design were used. A hydrophone was suspended 2 ft below the water gun to monitor the source signals. Hydrophones 1, 2, and 3 were suspended at a depth of 12 ft and at horizontal distances of 3, 13, and 23 ft, respectively, from the opposite side of air pipe frame.

The water gun is an implosive-type source. Water is ejected at high velocity through ports by compressed air, initial pressure of 2000 psi, which is subsequently vented to the surface. The principal source of energy in the generated sound wave arises from the collapse of voids caused by the outward thrust of water through each port which creates only a small precursor to the main sound pulse. Total energy is a function of the water chamber size. A 15-inch$^3$ chamber, the smallest available, was used; it provided ample energy. The water gun was selected because of negligible bubble oscillations which extend and complicate signals from water guns and explosive sources. Compressed air tanks and operating equipment for the water gun were mounted on the pier.

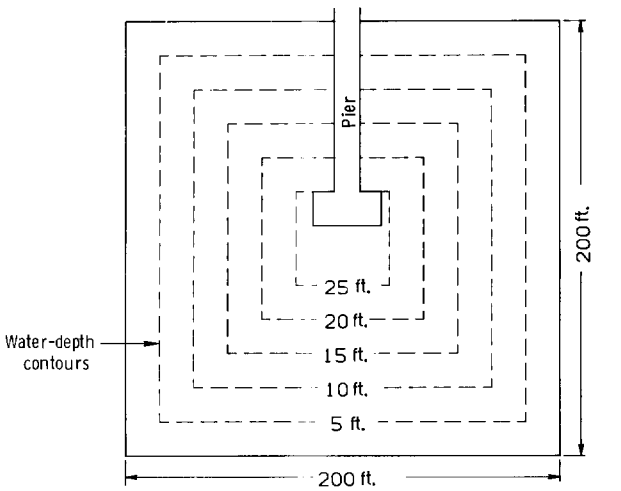


FIG. 1. Plan view of test pond showing depth contours and access pier.

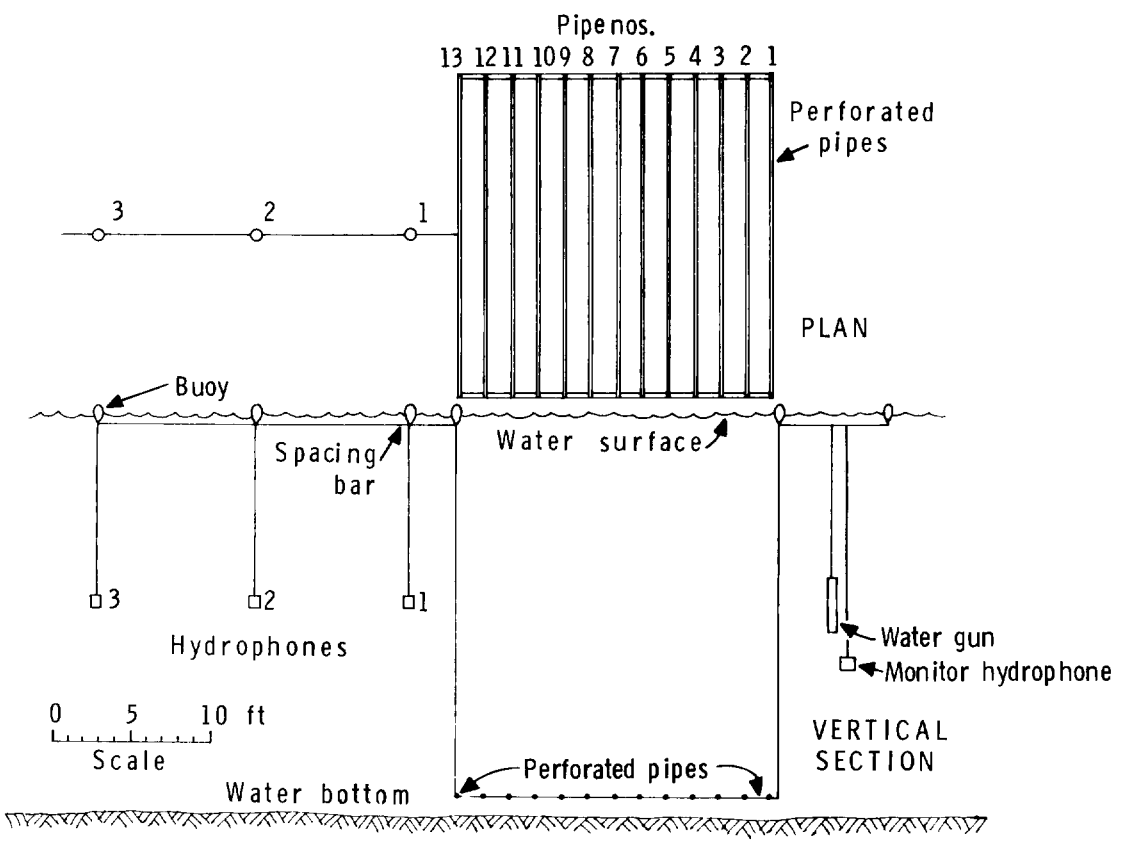


FIG. 2. Arrangement of perforated air pipes, water gun, and hydrophones employed at the test pond.

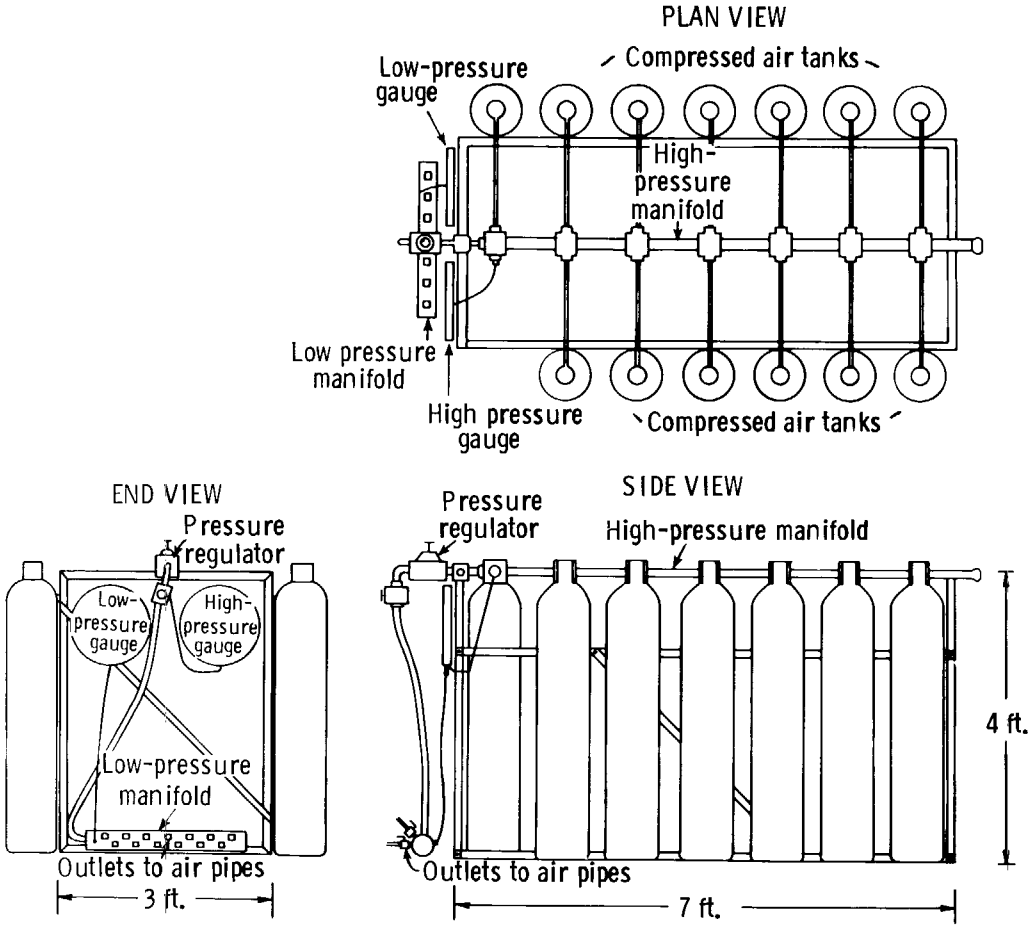


FIG. 3. System for supplying compressed air to the air pipes.

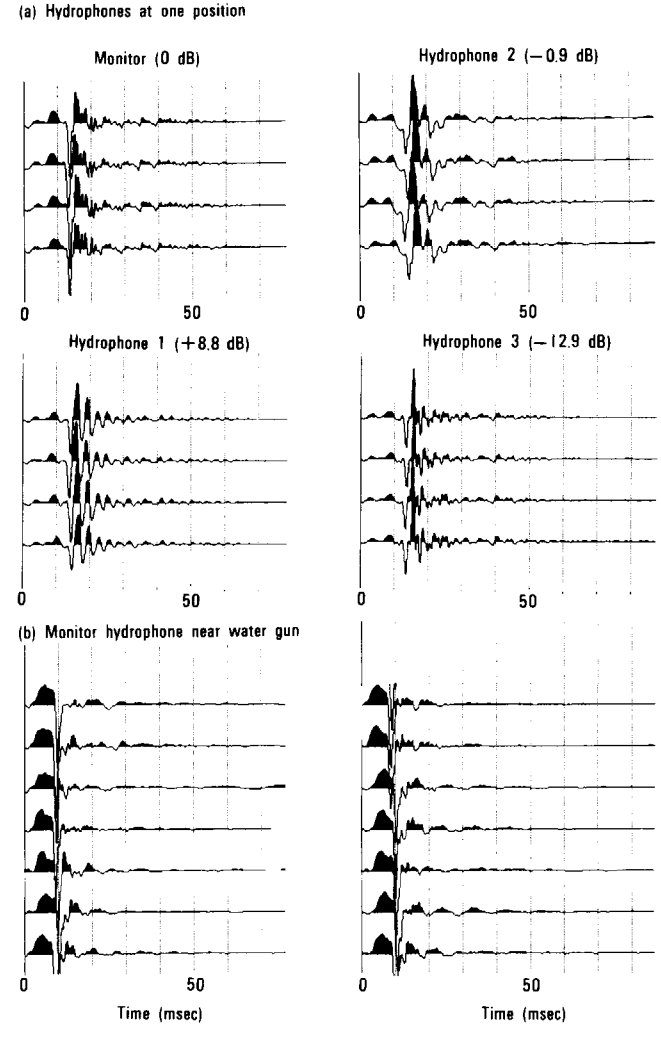


FIG. 4. Comparison of hydrophone responses and reproducibility of water gun signals.

Hydrophones were the pressure-sensitive, piezoelectric crystal type (GeoSpace MP-8F) with a rated sensitivity of 13 V/bar. Signals were recorded by a single-channel digital recorder at a sample rate of 4000/sec (0.25-msec sample interval). A specially designed switch permitted rapid connection of the recorder's single input channel to any one of the four hydrophones. Water gun firing was synchronized with signal recording.

The system used to supply compressed air to the air pipes is shown in Figure 3. Thirteen standard size (1.73 $ft^3$) compressed air tanks, at an initial pressure of 2000 psi, were used. Each tank supplied air to a central manifold, connected through an air pressure regulator to a low-pressure manifold. Each of the 13 air pipes was connected by a plastic tube through a valve to the latter. Thus, the air supply to each pipe could be turned on and off separately. An air pressure gauge was connected to the central manifold to monitor air tank pressure. A second gauge was connected to the low-pressure manifold for setting, by the regulator, the desired pressure of air supplied to one or more of the air pipes.

Four air pressures were used respectively in four sets of recordings by each of hydrophones 1, 2, and 3. These were 15 psi (slightly above ambient pressure at the depth of the air pipes), 25, 50, and 100 psi. At each pressure the water gun signal was recorded (by each of the three hydrophones in succession) initially without air-bubble curtains. Then pipes 1 through 13 (Figure 2) were supplied air in succession, commencing with pipe 1. Unfortunately, the air supply was exhausted before the sequence at 100 psi could be completed, only signals for pipes 1 through 6 being recorded.

Repeated recordings were made from the monitor hydrophone (Figure 2) to determine repeatability of the water gun source signal. Also, all four hydrophones were suspended at the same position and source signals were recorded to determine differences in response.

## EXPERIMENT RESULTS

### Reproducibility

For comparison of responses, the four hydrophones were grouped and suspended 12 ft deep and at a horizontal distance of 36 ft from the water gun (the position of hydrophone 2 in Figure 2). The water gun signal from each hydrophone was recorded several times. Typical signals are shown in Figure 4a. Duplication of signals recorded by the same hydrophone, indicative of the reproducibility of the water gun signal, appears to be satisfactory over the rather short time period (approximately 30 minutes) required for all recordings. Waveforms of signals from each hydrophone are similar; however, hydrophone 2 has a slightly narrower, lower frequency band-pass relative to the other hydrophones. Also, some of the high-frequency components in signals from the other three hydrophones do not duplicate on successive recordings. Hydrophone sensitivities vary

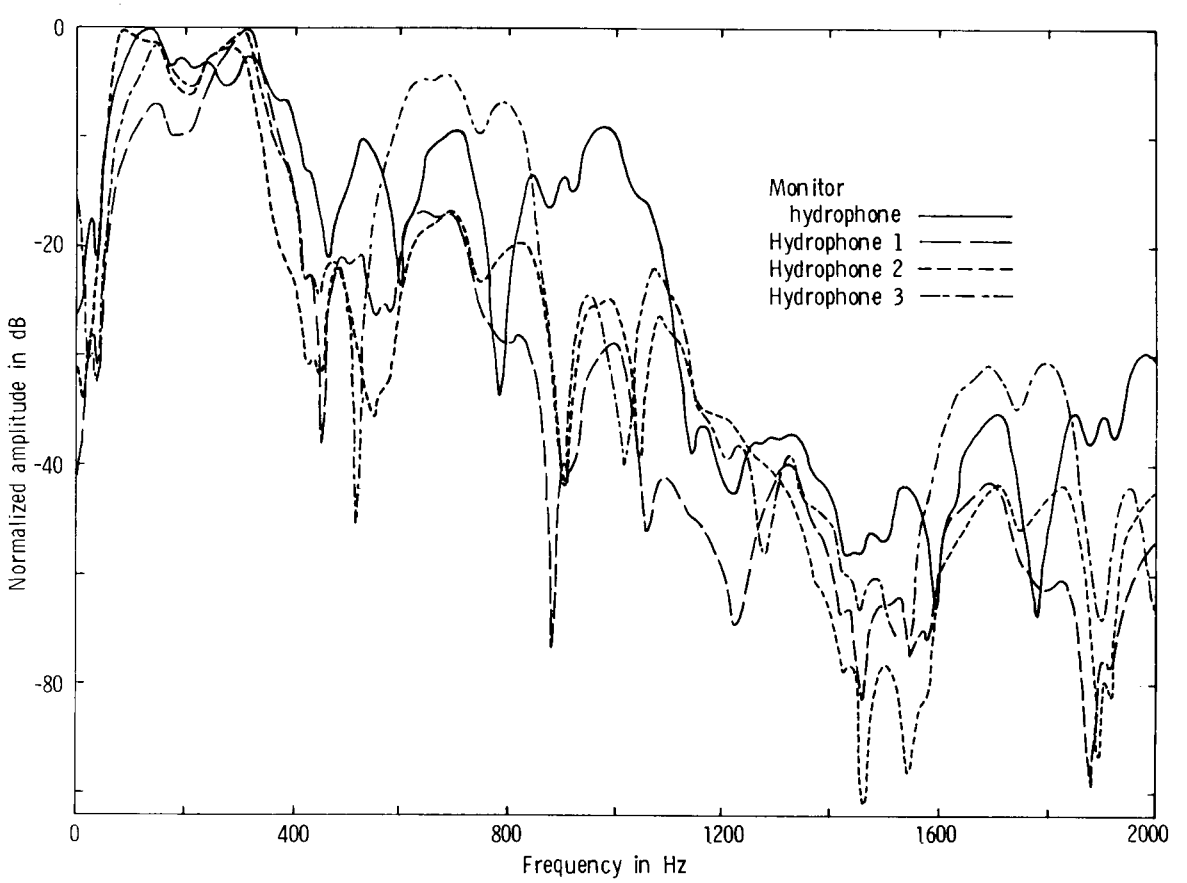


FIG. 5. Amplitude spectra of selected signals in Figure 4a from each of the four hydrophones at the same position.

from +8.8 dB for hydrophone 1 to −12.9 dB for hydrophone 3 relative to the monitor hydrophone. A typical amplitude spectrum for one signal from each of the hydrophones is shown in Figure 5. The abscissa extends to 2000 Hz, the Nyquist frequency. Throughout the experiment, which required approximately 6 hours, the monitor hydrophone positioned below the water gun (Figure 2) was recorded to monitor variation in the water gun signal. Those recordings are shown in Figure 4b. Differences in the signals are apparent and are likely responsible for some degradation of results. Maximum difference between signal times and a mean time in each trace set is ±1.0 msec. The rms of these differences is ±0.17 msec.

### Recorded signals

Signals recorded by hydrophones 1, 2, and 3 for each air pressure (15, 25, 50 and 100 psi) and for air-bubble curtains from pipes 1 to 13 activated in succession are displayed in Figure 6 in true relative amplitude; that is, amplitudes of signals from each hydrophone are relative to the signal amplitude on the bottom trace (no air curtains). The same signals are shown in Figure 7 where the maximum amplitude of each signal is nor-

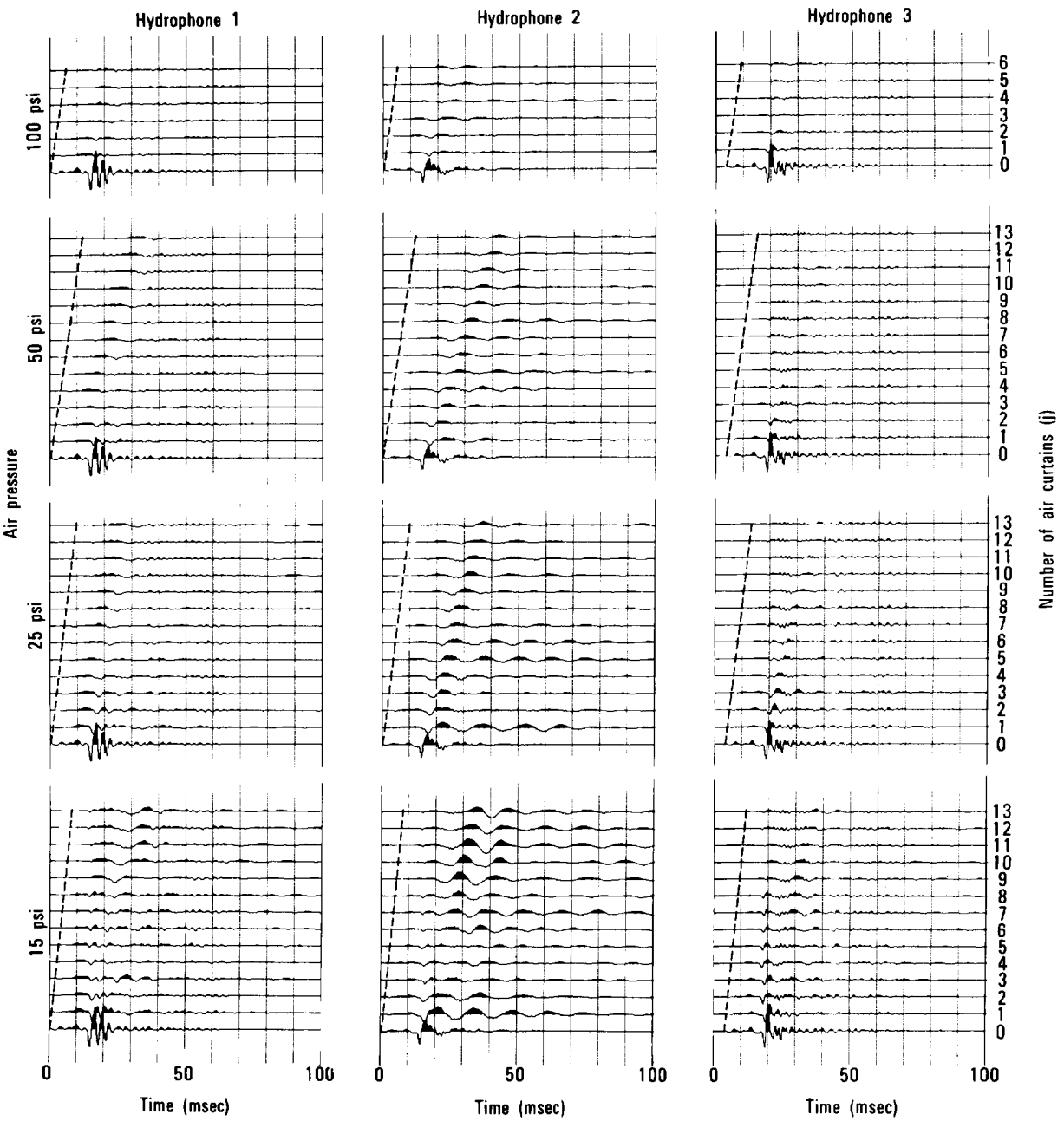


FIG. 6. Signals recorded by each of the three hydrophones, for each of four air pressures, and for air curtains from pipes 1 to 13 in succession, displayed in true relative amplitude. The dashed line on the left indicates signal onsets.

malized. The slanted dashed line on the left in each signal set of Figures 4 and 5 indicates the onset of each signal and is based on visual inspection of reproduced high gain signals. The onset is approximately 14 msec prior to the first main downbreak on the water gun signal recorded without air curtains (bottom trace in each signal set). This precursor is caused by the initial ejection of water, the downbreak occurring when the cavity created by the water ejection collapses. The narrower and lower frequency band-pass of hydrophone 2 is obvious. In Figure 6 the signal amplitudes appear to decrease greatly when a single air curtain (pipe 1) is activated and then remain nearly constant as air curtains are added successively. Also, the signals lengthen and become more complex as the number of air curtains increases.

## Signal transformations

The first step in signal processing was to correct for the variation in hydrophone response by removing the effect of this response from each signal. This was accomplished by first obtaining the Fourier transform $S_n(f)$ of all $n$ signals $S_n(t)$ in a set and dividing the transform $S_0(f)$ of the signal $S_0(t)$ recorded without air curtains into each transform of the remaining signals. These were then transformed to obtain the corresponding time signals. This process, of course, should also remove response of the digital recorder. The resulting signals for the sequence of successive air curtains are shown in Figure 8. Signals for an air pressure of 100 psi are not shown since these are an incomplete set and could not be used in the subsequent analysis. The bottom trace in each signal set results from division of the transform $S_0(f)$ by itself; thus, the corresponding time signal is a delta function at zero time as shown. It is apparent that the signals recorded by the three hydrophones at the same pressure and for the same number of air curtains are now much more similar than are those in Figure 7, indicating hydrophone responses have been removed to a large degree. The lower sensitivity of hydrophone 3, coupled with its higher frequency response, apparently introduces considerable noise. The signals in Figure 8 at the lowest air pressure (15 psi) have a distinctive narrow event at zero time which is most prominent on

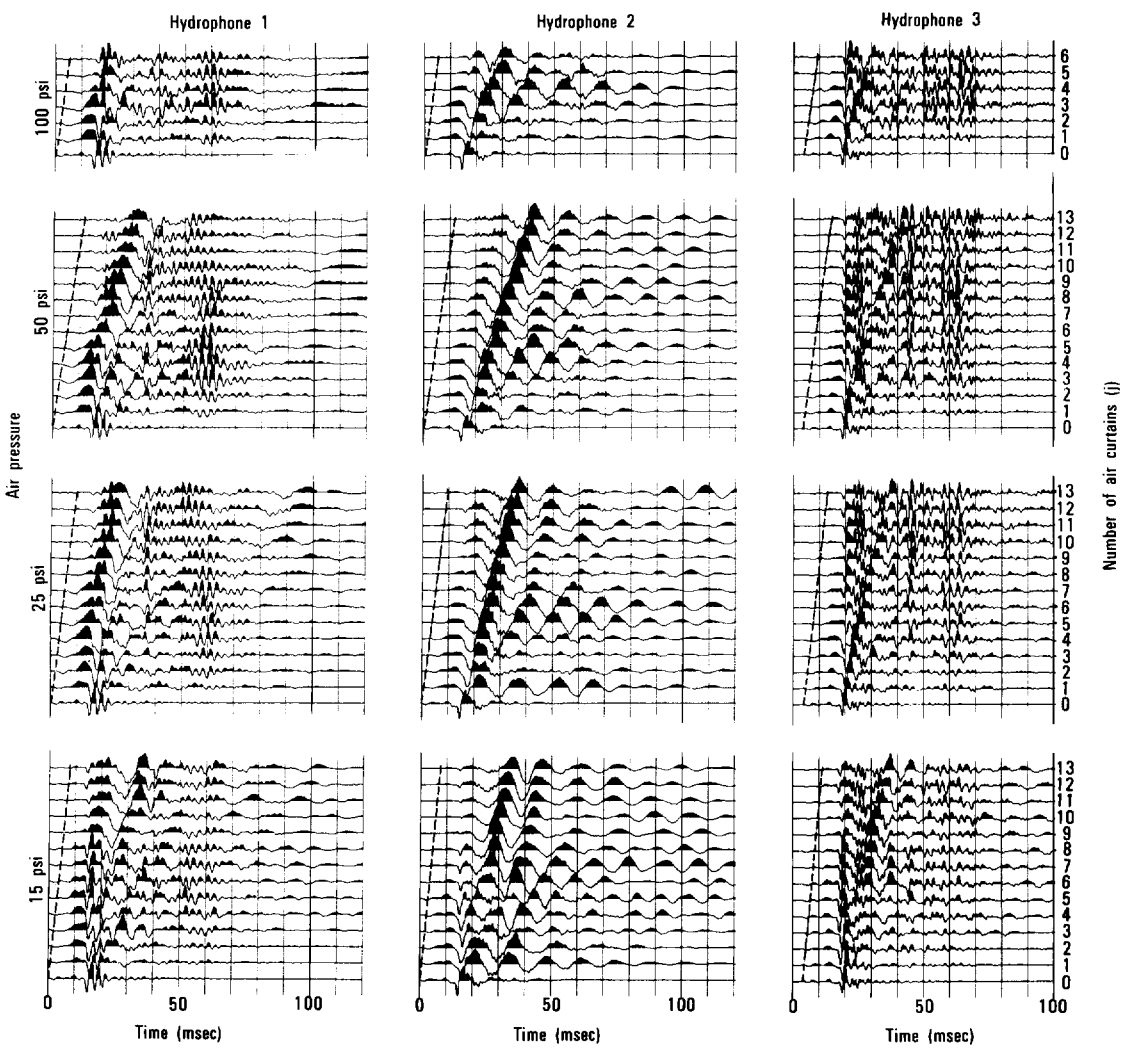


FIG. 7. Signals recorded by each of the three hydrophones, for each of four air pressures, and for air curtains from pipes 1 to 13 in succession, displayed with maximum amplitudes normalized. The dashed line on the left indicates signal onsets.

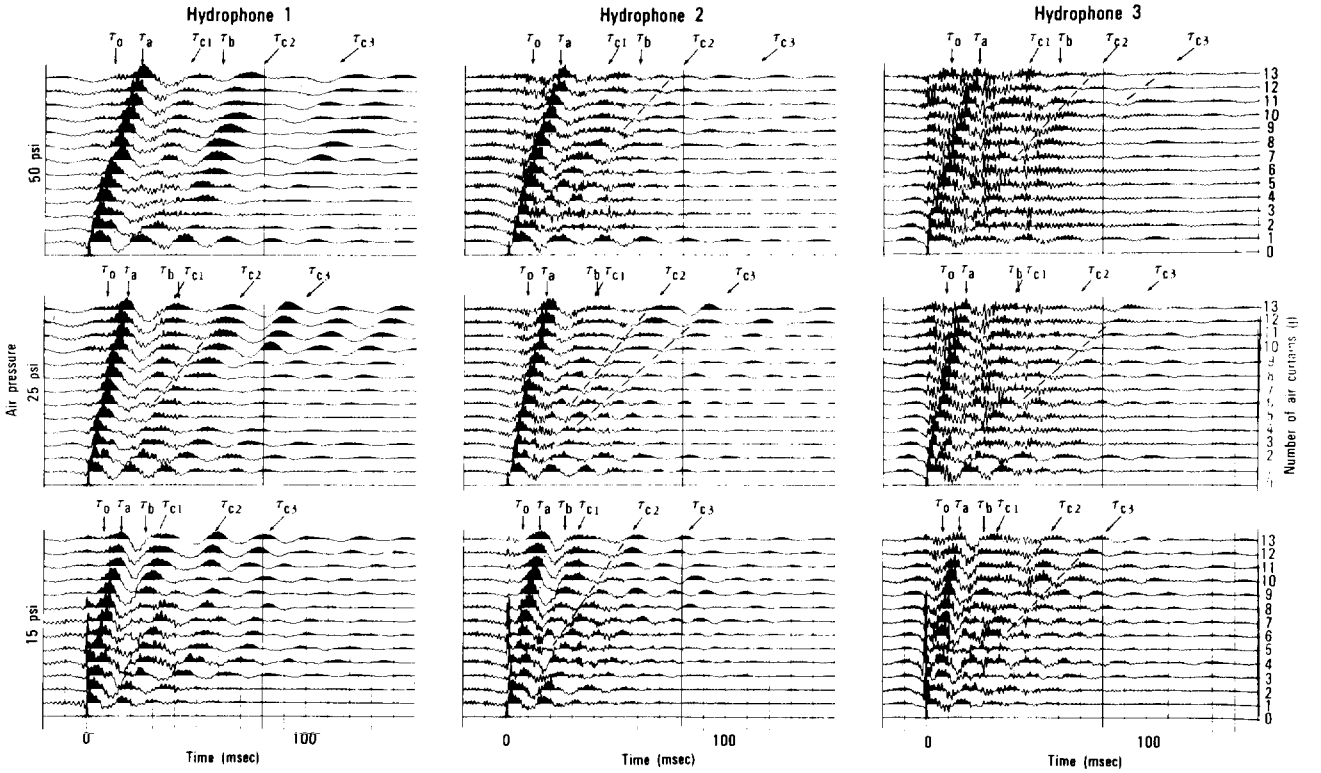


FIG. 8. Signals obtained by transforming the ratio of individual signal spectrum to the reference signal (no air curtains) spectrum in each signal set (Figure 7). Signals for an air pressure of 100 psi were not used since the sets are incomplete.

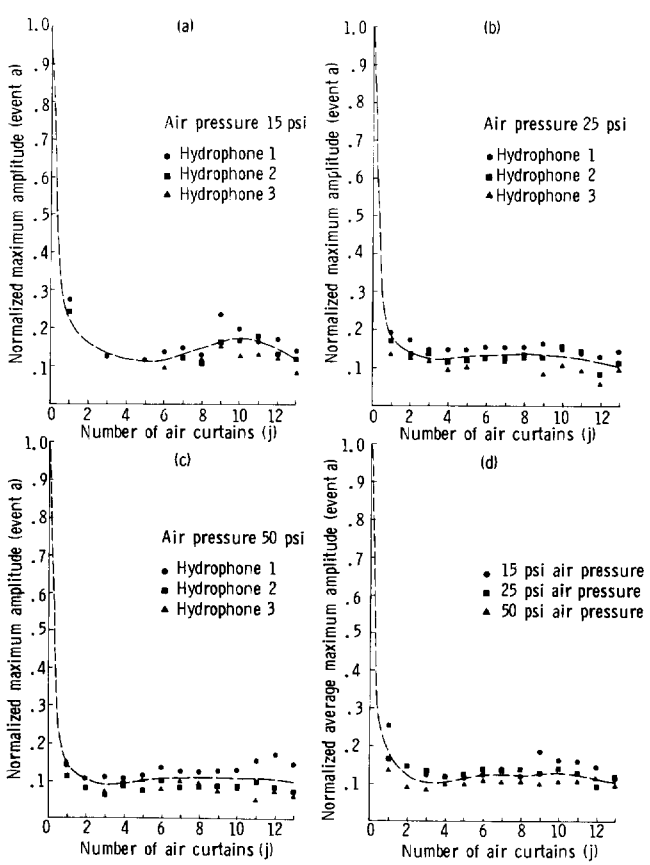


traces for 1 through 8 air curtains. It is quite possible that this represents sound energy traveling a refracted path through the subwater sediments. Thus, its traveltime would not be affected by the air curtains and would be nearly equal to traveltime of the reference signal $S_0(t)$. Reasons for its absence on other signal sets for air pressures 25 and 50 psi, except possibly on the hydrophone 3 signals, are unknown.

As mentioned above, the signals lengthen and become more complex as the number of consecutive air curtains increases. This indicates that reverberations of the sound energy are occurring. If the air curtains coalesce as consecutive pipes are activated, such reverberations would occur only between the vertical sides of the overall curtain, the traveltime between reflected events increasing by equal time intervals. If the air curtains do not coalesce, reverberations also would occur within each air curtain and between adjacent air curtains (bubble-free corridors). Since the reflection coefficient on each side of an air curtain is positive and on each side of the corridor between air curtains is negative, the polarity of reflections occurring within each is the same and remains constant.

FIG. 9. Normalized maximum amplitude of event a versus number $j$ of air curtains for air pressures of (a) 15 psi, (b) 25 psi, and (c) 50 psi. Also, (d) the normalized average maximum amplitude of event a recorded by the three hydrophones versus number of air curtains $j$ for each of the three air pressures.

The time and value of the maximum amplitude on each signal in Figure 8 was obtained by a computer program. Without exception, this maximum occurs on the event identified as a (delay time $\tau_a$) on each signal set in this figure. These amplitude maxima, normalized to the amplitude of the delta function on the bottom trace (no air curtains), are plotted versus number of air curtains in Figures 9a, 9b, and 9c for pressures 15, 25, and 50 psi, respectively. The normalized average amplitude recorded by the three hydrophones versus number of air curtains is also plotted (Figure 9d) for each of the three air pressures. As observed on the signal sets in Figure 6 (true relative amplitude), signal amplitude is decreased substantially by the first or first and second air curtains and remains nearly at the same level as additional air curtains are added. This is further evidence that reverberations are occurring since the number of multiple reflections would increase as the number of air curtains increases, thus overcoming, or at least moderating, the effect of transmission losses, energy absorption within the air curtains, and energy divergence. Delay times (time intervals between onset of direct signal without air curtains and event a maxima) of the maxima are plotted versus number of air curtains for each pressure in Figures 10a, 10b, and 10c. Generally, the times appear to increase linearly with number of air curtains for each pressure. Accordingly, straight lines were fit by regression analysis. Figure 10d is a summary plot showing the average delay time at each pressure for the three hydrophones and the associated lines. The rate of increase increases with pressure, the total delay time $\tau_a$ for 13 air curtains being 15.1, 17.6, and 23.8 msec for 15, 25, and 50 psi, respectively. As for the variation in amplitude, this variation in time of the maxima supports the observation that reverberations are occurring since the increase in multiple reflections with increasing number of air curtains would cause the overall signal to broaden in time and, consequently, delay the maximum.

## Reverberation systems

One system of reverberations, presumed to be principally responsible for event a, is shown in Figure 11. The multiple reflections are in corridors between air curtains. The ordinate is one-way traveltime and the abscissa is delay time (time after the direct or first arrival) in units of twice the one-way time $\tau_1$ in the bubble-free corridor. The one-way time $\tau_2$ through the air curtain is shown to be several times larger than $\tau_1$. This is because the expected velocity is much less than velocity in bubble-free water, although the curtain width is substantially less than the width of the corridor between air curtains. It was determined that the

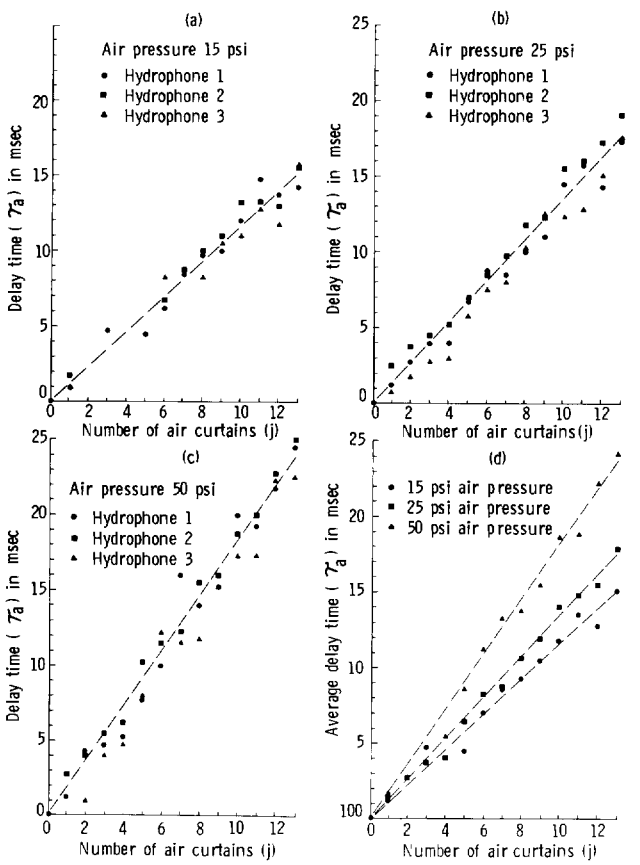


FIG. 10. Delay time($\tau_a$) of event a maximum versus number of air curtains ($j$) for air pressures of (a) 15 psi, (b) 25 psi, and (c) 50 psi. Also, (d) the average of these delay times for the three hydrophones versus number of air curtains $j$ for each of the three air pressures.

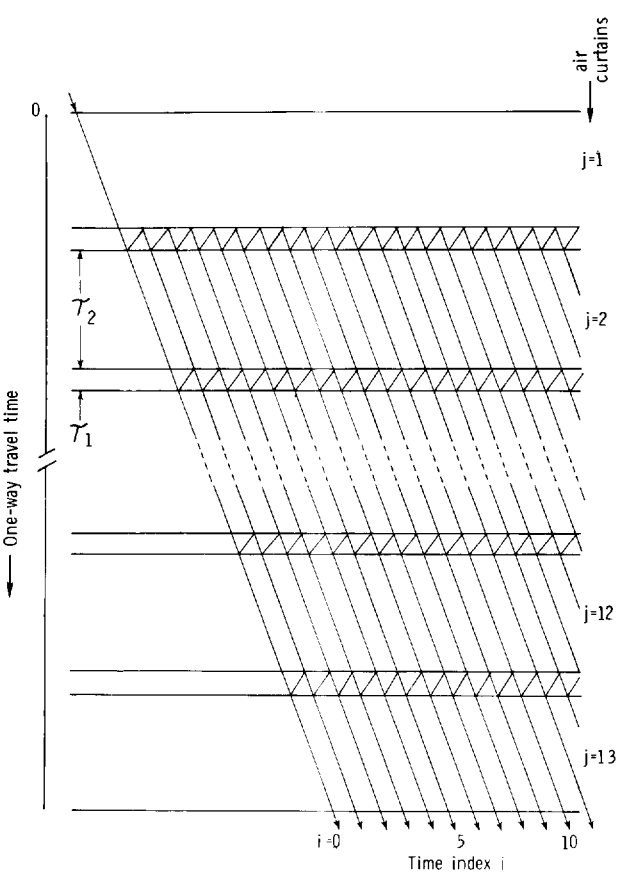


FIG. 11. Raypaths of multiple reflections believed responsible for event a. The time index $i$ is measured from the time of the direct (multiple-free) arrival. The time unit is $2\tau_1$, twice the one-way time through the corridor between air curtains.

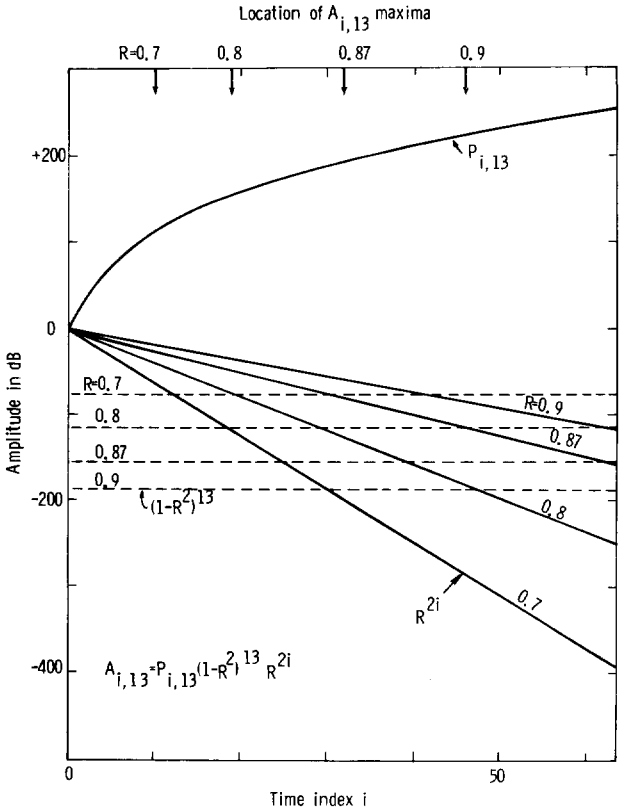


FIG. 12. Amplitude of the three factors $P_{i,j}$, $(1 - R^2)^j$, and $R^{2i}$, the product of which determines the amplitude $A_{i,j}$ of event a, versus time index for 13 air curtains ($j = 13$) and for reflection coefficients $R$ as indicated. The location of event a maximum for each reflection coefficient also is shown.

number of equal time raypaths $P_{i,j}$, where $i (i = 0, 1, 2, 3, \ldots)$ is the time index and $j$ is the number of air curtains ($j = 2, 3, \ldots, 12, 13$), is given by the product of a matrix $Q_{i,j}$ and its transpose

$$P_{i,j} = Q_{i,j}Q^T_{i,j}$$

$$= \begin{vmatrix} 1 & 0 & 0 & 0 & 0 & \cdots \\ 1 & 1 & 0 & 0 & 0 & \cdots \\ 1 & 2 & 1 & 0 & 0 & \cdots \\ 1 & 3 & 3 & 1 & 0 & \cdots \\ 1 & 4 & 6 & 4 & 1 & \cdots \\ \cdots & \cdots & \cdots & \cdots & \cdots & \cdots \end{vmatrix} \cdot \begin{vmatrix} 1 & 1 & 1 & 1 & 1 & \cdots \\ 0 & 1 & 2 & 3 & 4 & \cdots \\ 0 & 0 & 1 & 3 & 6 & \cdots \\ 0 & 0 & 0 & 1 & 4 & \cdots \\ 0 & 0 & 0 & 0 & 1 & \cdots \\ \cdots & \cdots & \cdots & \cdots & \cdots & \cdots \end{vmatrix}$$

$$= \begin{vmatrix} 1 & 1 & 1 & 1 & 1 & \cdots \\ 1 & 2 & 3 & 4 & 5 & \cdots \\ 1 & 3 & 6 & 10 & 15 & \cdots \\ 1 & 4 & 10 & 20 & 35 & \cdots \\ 1 & 5 & 15 & 35 & 70 & \cdots \\ \cdots & \cdots & \cdots & \cdots & \cdots & \cdots \end{vmatrix}.$$

[The elements of the matrix $Q_{i,j}$ are equivalent to the coefficients of the series approximation to the binomial $(x + y)^n$.] For plane waves parallel to the air curtains, the amplitude $A_{i,j}$ is given by

$$A_{i,j} = P_{i,j}(1 - R^2)^j R^{2i}, \tag{1}$$

where $R$ is the reflection coefficient at the interface between the air curtain and bubble-free corridor. The factor $(1 - R^2)^j$ accounts for transmission losses, and the factor $R^{2i}$ accounts for multiple reflections within the bubble-free corridors. These two factors and $P_{i,j}$ are plotted versus delay time index $i$ in Figure 12 for 13 air curtains ($j = 13$) and reflection coefficients of 0.7, 0.8,

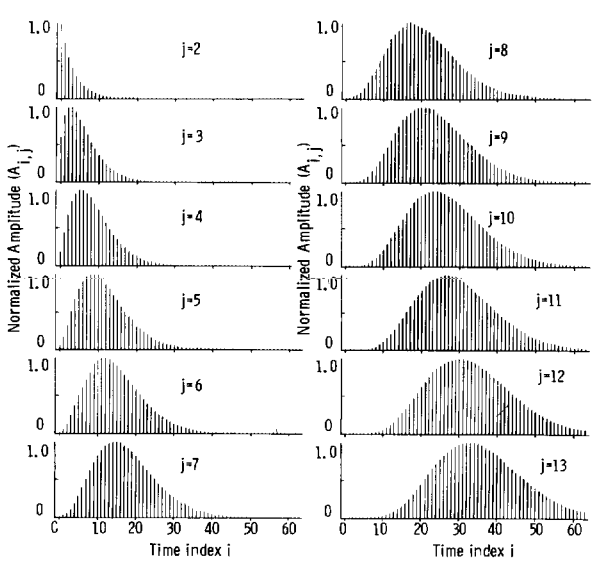


FIG. 13. Synthetic event a for a reflection coefficient $R$ of 0.87 and for 2 to 13 air curtains. The time is in units of $2\tau_1$ (twice the one-way time through a bubble-free corridor).

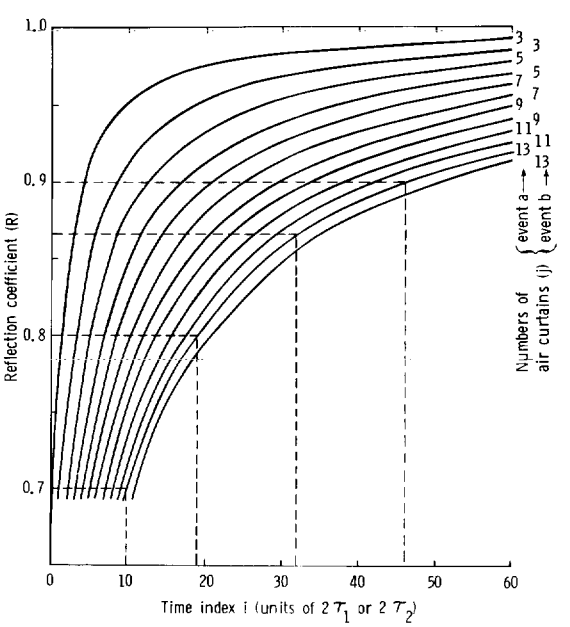


FIG. 14. Nomogram for determining time index $i$ at event a and event b maxima given the reflection coefficient $R$ and number of air curtains $j$. Times of event a maxima are indicated (dashed lines) for reflection coefficients shown in Figure 12.

**Table 1. Signal onset time $\tau_0$ and time $\tau_a$ of event a maximum for 13 air curtains ($j = 13$).**

| Air pressure (psi) | Times (msec) $\tau_0$ | $\tau_a$ |
|---|---|---|
| 15 | 7.5 | 15.1 |
| 25 | 9.5 | 17.6 |
| 50 | 11.5 | 23.8 |

0.87, and 0.9. The transmission loss term is constant. The amplitude maximum is created by increasing $P_{i,13}$ and decreasing $R^{2i}$. Two additional losses are not accounted for, namely, spherical divergence and absorption in the air curtains. The former cannot be determined accurately until the air curtain width (and thereby also the bubble-free corridor width) is known. However, it was determined after this width had been estimated that spherical divergence would modify time of the event a maximum negligibly. Energy absorption in the air curtains in the case of event a is constant with time index $i$ for a given number of air curtains (Figure 11) and, thus, cannot alter time of the event a maximum. As a demonstration of this phenomenon, a synthetic event a was computed (Figure 13) for $R = 0.87$ and for numbers of air curtains $j$ from 2 to 13. The amplitude of each pulse is normalized to its maximum amplitude. As expected, the event broadens with increasing $j$ and the maximum is delayed progressively. The time index $i$ of the maximum for $j = 13$ is 32 and is indicated in Figure 12 for $R = 0.87$.

The time of the maximum was computed for a variety of reflection coefficients in the range $0.7 \leq R < 1.0$ and for numbers of air curtains from 2 to 13. From these data the nomogram in Figure 14 was prepared where the reflection coefficient $R$ is plotted versus time index $i$ for each number $j$ of air curtains. Curves for $j = 1$ and $j = 2$ are not shown since the time index of the maximum is 0, that is, the maximum occurs at the onset of event a for all $R$ and is the direct arrival (no multiple reflections) from the source. Index times of the maxima for $j = 13$ are indicated for the reflection coefficients shown in Figure 12 on which these times are also indicated. For each $j$ the time of the maximum increases nonlinearly with increasing $R$ at an increasing rate. For a given $R$, time of the maximum increases linearly (from $j = 2$, the ordinate) with increasing $j$. As noted above, the observed times of the event a maxima appear to be linearly related to $j$ (Figure 10).

The nomogram in Figure 14 can also be used to predict times of the maxima of the event created by reverberations in the air curtain (Figure 15), which is designated event b. For this event the time must be in units of $2\tau_2$, twice the one-way traveltime through an air curtain. Since this time is appreciably greater than $\tau_1$, the one-way traveltime in the bubble-free corridor, event b will be considerably broader than event a and its maximum will be delayed progressively more than is the maximum of event a with increasing $j$. For event b, the curves on the nomogram (Figure 14) must be redesignated as shown since $j$ will vary from 1 to 13 (rather than from 2 to 13 for event a), the time index for $j = 1$ always being 0. Unlike event a, energy absorption in the air curtains, not accounted for in the nomogram, likely would reduce the time of the event b maximum from that predicted by the nomogram since multiple reflections occur within the energy-absorbing air curtains. Event b, however, was not used in subsequent analysis.

## Air curtain characteristics

Now that the nature of event a has been established, it is possible to determine for each air pressure the physical width of the air curtain and of the bubble-free corridor, reflection coefficient at the interface, and velocity in the air curtain from the observed times of the event a maxima $\tau_a$ and of the signal onset $\tau_0$ relative to the onset time of the reference signal (signal recorded without air curtains). Times $\tau_0$, as mentioned, were determined by visual inspection of reproduced high-gain original (unprocessed) signals. Times for 13 air curtains ($j = 13$) listed in Table 1 were used. An iterative procedure was employed as follows:

(1) Assume a reflection coefficient $R$ value.
(2) Obtain time index $i$ of event a maximum for $j = 13$ from $R$ versus $i$ nomogram (Figure 14).
(3) Compute one-way traveltime $\tau_1$ in bubble-free corridor from $\tau_1 = 0.5\,(\tau_a - \tau_0)/i$.
(4) Compute width $\ell_1$ of bubble-free corridor from $\ell_1 = c_0\tau_1$, where $c_0 = 4870$ ft/sec.
(5) Compute velocity $c$ in air curtain from

$$\frac{1}{c} = \frac{\tau_0}{13}\,\frac{1}{\ell_2} + \frac{1}{c_0}$$

and one-way traveltime $\tau_2$ in the air curtain from $\tau_2 = \ell_2/c_2$.

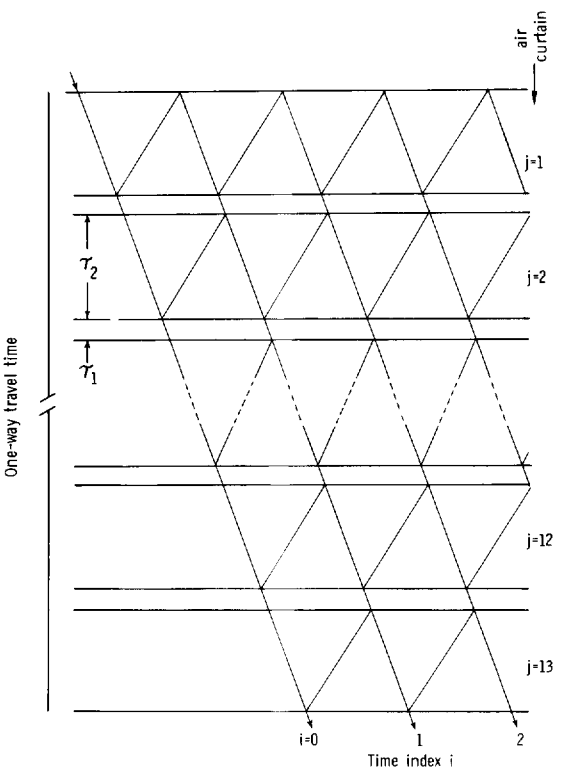


FIG. 15. Raypaths of multiple reflections occurring within the air curtains which create event b. The time index $i$ is measured from the time of the direct (multiple-free) arrival which is the same time reference for the event a time index (Figure 11). The time unit, however, is $2\tau_2$, twice the one-way time through the air curtain rather than $2\tau_1$.

**Table 2. Parameters obtained by iterative computation procedure based on observed signal onset times $\tau_0$ and times $\tau_a$ of event a maxima for 13 air curtains.**

| Air pressure (psi) | Time index ($i$) | Width (ft) | | One-way traveltime (msec) | | Velocity ($c$) in air curtain (ft/sec) | Reflection coefficient ($R$) |
|---|---|---|---|---|---|---|---|
| | | Air curtain ($\ell_2$) | Bubble-free corridor ($\ell_1$) | Air curtain ($\tau_2$) | Bubble-free corridor ($\tau_1$) | | |
| 15 | 13 | 0.467 | 1.200 | 0.675 | 0.250 | 692 | 0.747 |
| 25 | 18 | 0.467 | 1.200 | 0.825 | 0.250 | 563 | 0.790 |
| 50 | 22 | 0.467 | 1.200 | 0.975 | 0.250 | 475 | 0.820 |

(6) Compute reflection coefficient $R$ from $R = (c_0 - c)/(c_0 + c)$. (The densities $\rho$ and $\rho_0$ are not sufficiently different to affect $R$ significantly.)

(7) Compare computed reflection coefficient [step (6)] with assumed reflection coefficient [step (1)] and repeat steps (1) to (6) with new assumed reflection coefficient.

It was possible to reduce the iterations to as few as three by plotting the assumed $R$ versus the computed $R$ and noting where a line joining these crosses the line of equality (line of unit slope through the origin). Results are given in Table 2. Widths of the air curtain and of the bubble-free corridor do not appear to vary. Velocity in the air curtain decreases and reflection coefficient increases with increasing air pressure, as would be expected. Traveltime in the air curtain is from about 3 to 4 times the traveltime in the bubble-free corridor, although the air curtain width is about four-tenths the width of the latter.

The derived traveltimes in the air curtains and in the bubble-free corridors (Table 2) may now be used to determine times of the event b maxima created by reverberations in the air curtain illustrated in Figure 15, and also the onset times of overall multiple reflections, designated events c, between the outer interfaces of the outermost air curtains as shown in Figure 16. Times of event b maxima for 13 air curtains were obtained by first determining time index $i$ from the nomogram (Figure 14) for the appropriate reflection coefficient $R$ (Table 2) and for $j = 13$ (event b). The times $\tau_b$ of the event b maxima then are given by

$$\tau_b = \tau_0 + 2i\tau_2. \tag{2}$$

The times $\tau_0$ and $\tau_2$ are given in Tables 1 and 2, respectively. The time index $i$ and computed times $\tau_b$ are listed in Table 3.

As mentioned above, however, the times $\tau_b$ are likely too long since energy absorption in the air curtains is not accounted for. Onset times $\tau_c$ of the overall multiples ($j = 13$) are given by

$$\tau_{cn} = (2n + 1)(12\tau_1 + 13\tau_2) - 20/c_0, \qquad n = 1, 2, 3, \ldots, \tag{3}$$

where $n$ is the order of the multiple and the last term is for correction to the time reference (arrival time of direct wave without air curtains). The times $\tau_{cn}$ for the first-, second-, and third-order multiples are also listed in Table 3.

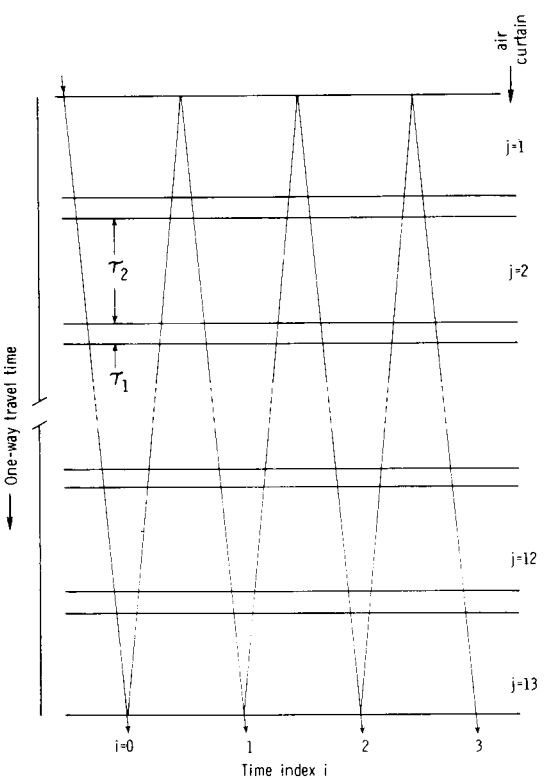


FIG. 16. Raypaths of multiple reflections occurring between the outer interfaces of the outermost air curtains. The time index $i$ is measured from the time of the direct (multiple-free) arrival which is the same time reference for events a and b (Figures 11 and 15). The time unit is $2[j\tau_1 + (j - 1)\tau_2]$.

### Comparison of predicted and observed event times

The computed time positions of events b and c are indicated on the transformed signal sets in Figure 8. With the exception of hydrophone 1, 25 psi, signal set, event b does not coincide with the amplitude maxima of a second pulse. Possibly the reasons are two-fold: (1) Frequency-dependent energy absorption in the air curtains has not been accounted for and (2) the first-order multiple (event c1) interferes with event b and, thus, neither can be identified. By contrast, the second-order multiple (event c2) is clearly visible on at least two signal sets, the hydrophone 2, 15 and 25 psi sets. Evidence of the third-order multiple (event c3) appears unmistakable on the hydrophone 1, 15 psi set. This appearance of the second- and third-order overall multiples at predicted positions indicates that the derived one-way traveltimes $\tau_1$ and $\tau_2$, and air-curtain width $\ell_2$ are nearly correct.

Table 3. Times of maximum amplitude of event b and onset times of first-, second-, and third-order overall multiples (events c) for 13 air curtains ($j = 13$).

| Air Pressure (psi) | Event b | | Events c (overall multiples) | | |
|---|---|---|---|---|---|
| | ($i$) | ($\tau_b$) (msec) | First ($\tau_{c1}$) (msec) | Second ($\tau_{c2}$) (msec) | Third ($\tau_{c3}$) (msec) |
| 15 | 14 | 26.4 | 31.1 | 54.8 | 78.3 |
| 25 | 19 | 40.8 | 37.1 | 64.5 | 92.0 |
| 50 | 25 | 60.3 | 42.9 | 74.3 | 105.6 |



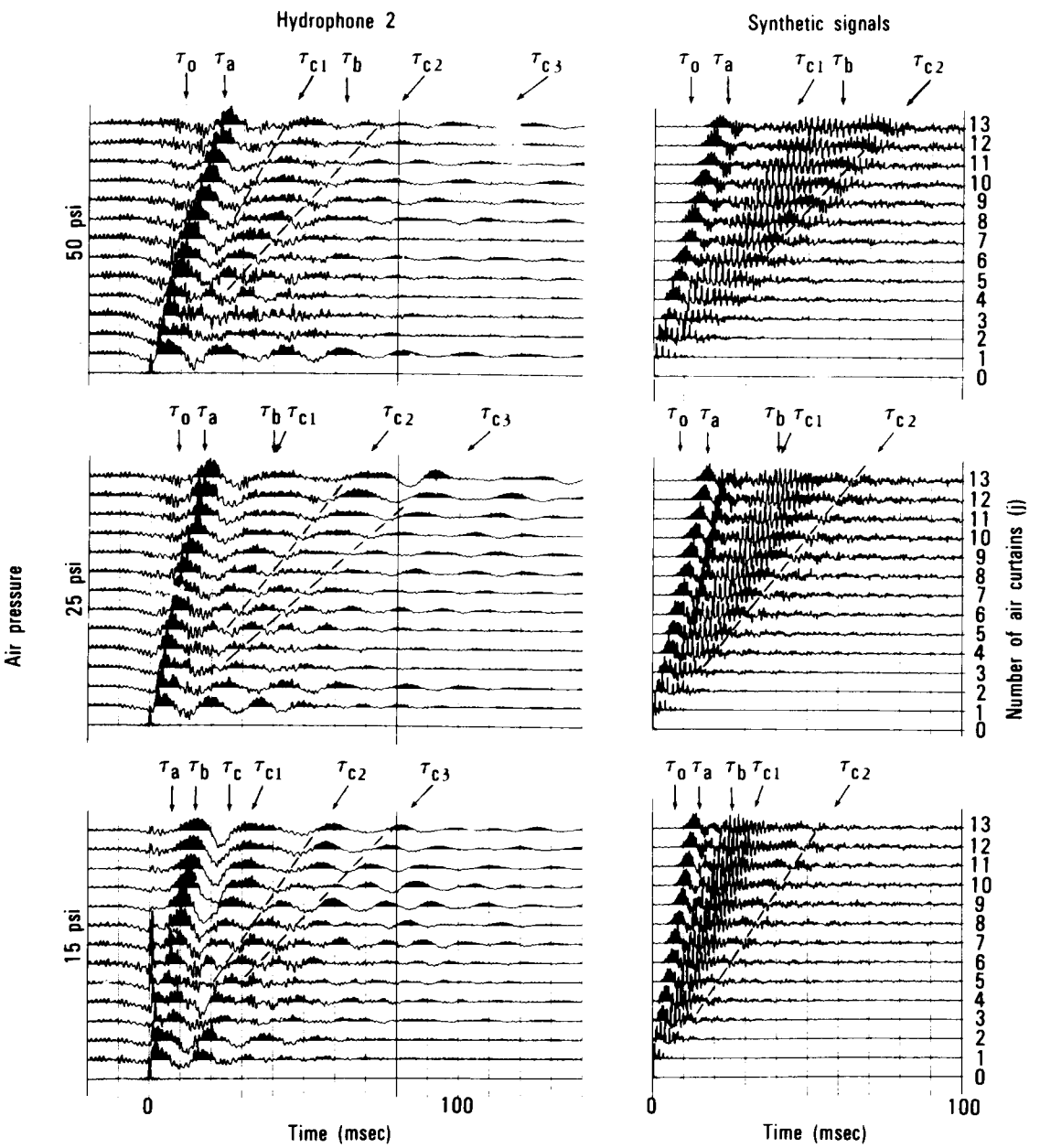


FIG. 17. Synthetic signals (right) for successive pipe sequence at each of the three air pressures with the corresponding hydrophone 2 signals.

**Table 4. Fractional air volume at a water depth of 12 ft determined from an air-flow test and from the velocity-fractional air volume function [equation (14) Domenico, (1982) for the derived velocities (Table 2).**

| Air Pressure (psi) | Fractional air volume ($s$) | | | |
|---|---|---|---|---|
| | From air-flow test | | From derived velocities | |
| | $r$ = 0.002 ft | $r$ = 0.014 ft | $f$ = 50 Hz | $f$ = 2500 Hz |
| 15 | 0.011 | 0.007 | 0.004 | 0.003 |
| 25 | 0.022 | 0.015 | 0.006 | 0.005 |
| 50 | 0.063 | 0.041 | 0.009 | 0.007 |



## Synthetic signals

Now that apparently satisfactory acoustic model parameters have been derived (Table 2), synthetic signals may be computed for each configuration of air curtains at each of the three air pressures. These signals were derived by following a procedure described by Grant and West (1965) based on a matrix formulation by Thomson (1950). A plane wave parallel to a series of plane layers, each of which may differ in elastic properties, is assumed. The procedure, described in Appendix A, is simplified considerably for the models employed here. The set of models for each of the three air pressures consists of two layer types, namely, the air curtain and the bubble-free corridor between air curtains. Further, thickness of each layer type is the same for all three model sets, the only difference between sets being the velocity and density of the air curtain. It was necessary to use a sample interval of 0.025 msec for accurate time positioning of reflection coefficients in construction of the synthetic signals.

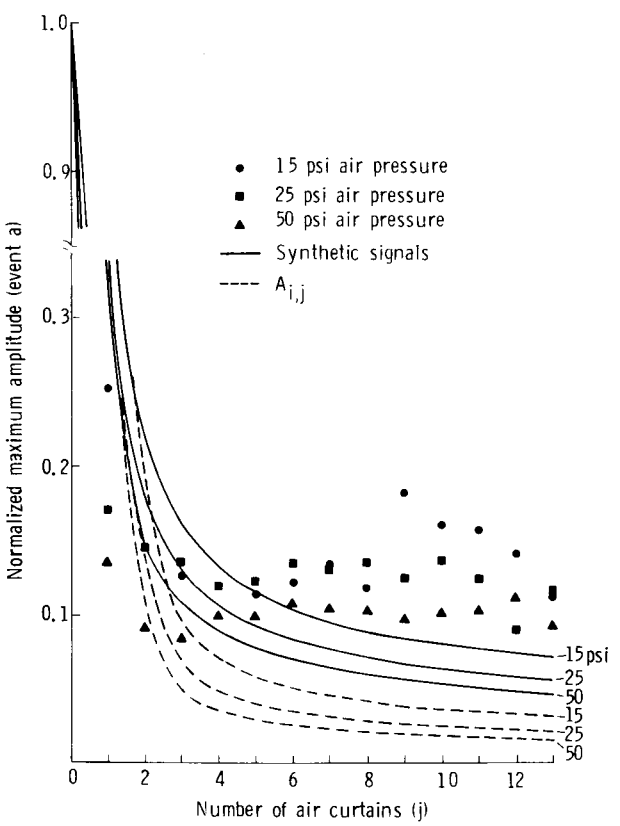


FIG. 18. Event a normalized maximum amplitude versus number of air curtains from synthetic signals (solid lines), theoretical air curtain reverberation system (dashed lines), and averaged event a amplitudes of signals recorded by the three hydrophones (plotted points), all for each of the three air pressures.

Synthetic signals for the successive-pipe sequence and for each of the three air pressures are displayed in Figure 17 along with corresponding hydrophone 2 signals. The correspondence is believed satisfactory considering that (1) the synthetic traces are for plane waves and (2) the models do not account for absorption in the air curtains nor reflections from the air/water and water/sediment interfaces. However, such reflections are not evident on signals recorded without air curtains (e.g., Figure 4a) and, as shown in Appendix B, beyond the primary and second-order reflections (raypaths 1, 2, and 3, 4 in Figure B-1) are, theoretically, severely attenuated. This is demonstrated by the reflection spike sequence in Figure B-2a and the convolved monitor hydrophone signal (trace a in Figure B-2b). The synthetic signals correspond to the hydrophone 2 signals (Figure 17) in that event a is prominent, although considerably narrower, events b and c1 cannot be distinguished, and event c2 is distinctive. On the contrary, the hydrophone 2 signals appear to persist longer and have low-frequency components (periods of about 15 to 20 msec), especially prominent on the signals for 1 and 2 air curtains, which are not present on the synthetic signals. Perhaps these result from incomplete removal of hydrophone response.

## Event a theoretical and measured amplitudes

Theoretical maximum amplitudes of event a are given by equation (1) for reverberations in the bubble-free corridors between air curtains (Figure 11) and also may be obtained from synthetic signals (Figure 17). These amplitudes normalized to the amplitude of the first arrival without air curtains are indicated by the curves in Figure 18 on a graph of amplitude versus number of air curtains. Also shown are averaged amplitudes of event a on signals recorded by the three hydrophones for each of the three air pressures (shown previously in Figure 9d). Differences are accentuated by expansion of the amplitude scale. The theoretical curves for the reverberation system (dashed lines) are below those for synthetic signals (solid lines), indicating that the former does not account for other signal paths contributing to event a. Beyond the first few air curtains the observed amplitudes exceed the theoretical amplitudes, due most likely to the inadequacy of the models and to unknown backscattered signals within the pond. Measured amplitudes appear to decrease with increase in air pressure as predicted by the theoretical curves.

### Fractional air saturation

Prior to the signal recordings, air flow rates were determined by observing the pressure decline, as well as the temperature change, of the air supply system (Figure 3) as air was supplied to one of the 13 pipes (Figure 2) at constant pressures of 15, 25 and 50 psi. The air flow rates determined, corrected to the pressure and temperature at a water depth of 12 ft, were 0.051, 0.101, and 0.284 $ft^3$/sec for air pressures of 15, 25, and 50 psi, respectively. The fractional air saturation $s$ is given by

$$s = \frac{F}{\sigma v}, \tag{4}$$

where $F$ is the flow rate in $ft^3$/sec, $\sigma$ is the cross-sectional area in $ft^2$ through which the bubbles flow, and $v$ is bubble velocity in ft/sec. The area is given by the air-curtain width $\ell_2$ determined above (Table 2) multiplied by the pipe length (20 ft). The bubble velocity may be obtained from a bubble velocity (rate-of-rise) versus radius graph (Figure 19) developed by Pekeris (1942) from laboratory measurements. As shown in Figure 19, the velocities for the two extremes of bubble size are 0.484 ft/sec for a bubble radius of 0.002 ft (hole radius) and 0.735 ft/sec for a bubble radius of 0.014 ft (6.48 times the hole radius). The fractional air volumes determined from equation (4) are listed in Table 4 for each of the two bubble radii and for each of the three air pressures. Also listed are fractional air volumes at 50 and 2500 Hz derived from equation (14) (Domenico, 1982), for velocities given in Table 2 and constants given in Table 2 of Domenico (1982). Fractional air volumes derived from the air flow test are from about two to nine times greater than those derived from velocities, the difference increasing with air pressure. Reasons for this discrepancy could not be established definitely. In limited laboratory experiments, it was established that bubble velocity depends upon the bubble production rate (number of bubbles generated per second), which increases as the air pressure increases, as well as on bubble size. It was observed that the velocity increased from approximately 0.83 to 1.25 ft/sec as the bubble production rate was increased from one to 15 bubbles/sec by increasing the air pressure. The bubble velocity versus radius curve in Figure 19 is for isolated bubbles, and the lower velocity (0.83 ft/sec) agrees well with the curve at the observed bubble radius (approximately 0.02 ft). The increase is much greater than accounted for by an increase in bubble size with increasing pressure. Thus, bubble motion appears to be interactive, and the velocities obtained from the curve in Figure 19 are likely too low, implying that the fractional air saturations derived from the air flow test (listed in Table 4) are erroneously high. Another cause of the discrepancy between fractional air volumes by the two methods may be variation in air-bubble density, both vertically and horizontally. Thus, the fractional air volume derived from acoustic wave velocities is likely only an *effective* value and would vary as depth of the water gun and hydrophones is varied.

### Absorption

The presence of dominant reverberations in the bubble-free corridors between air curtains precluded meaningful determination of frequency-dependent absorption in the latter. It is possible only to estimate this absorption by synthetically expanding the width of the air curtains until these coalesce, thereby eliminating the bubble-free corridors. Then the theoretical absorption [equation (10), Domenico, 1982] may be applied for a range of plausible parameters (i.e., air saturation and bubble radius).

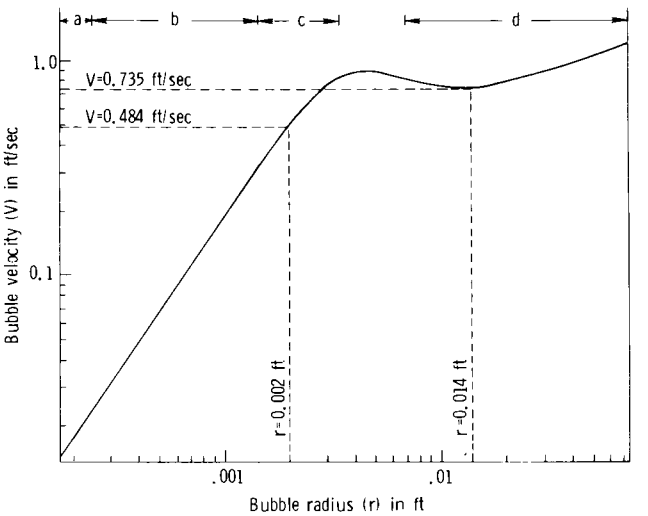


FIG. 19. Bubble velocity (rate of rise) in water versus bubble radius developed by Pekeris (1942) from laboratory measurements. The ranges of bubble radii shown at the top of the graph are with reference to observed bubble motion and shape as follows: $a$ = rectilinear motion, spherical shape; $b$ = helical and twisting motion, flattened shape; $c$ = irregular motion and shape; $d$ = rectilinear motion, distorted mushroom shape.

**Table 5. Bubble-free corridor width $\ell_1$, air-curtain width $\ell_2$, and one-way traveltime $\tau_1$ in the bubble-free corridor and $\tau_2$ in the air curtains for each of four air-curtain configurations (oroginal and three stages).**

| | Width (ft) | | Traveltime (msec) | | | |
|---|---|---|---|---|---|---|
| | | | $\tau_1$ | $\tau_2$ | | |
| Configuration | $\ell_1$ | $\ell_2$ | | 15 psi | 25 psi | 50 psi |
| Original | 1.200 | 0.467 | 0.250 | 0.675 | 0.829 | 0.983 |
| Stage 1 | 0.800 | 0.867 | 0.167 | 1.253 | 1.540 | 1.825 |
| Stage 2 | 0.400 | 1.267 | 0.083 | 1.831 | 2.250 | 2.667 |
| Stage 3 | 0.000 | 1.667 | 0.000 | 2.409 | 2.961 | 3.509 |
| Reflection coefficient ($R$) | | | | 0.747 | 0.790 | 0.820 |
| Velocity ($c$) in ft/sec | | | | 692 | 563 | 475 |

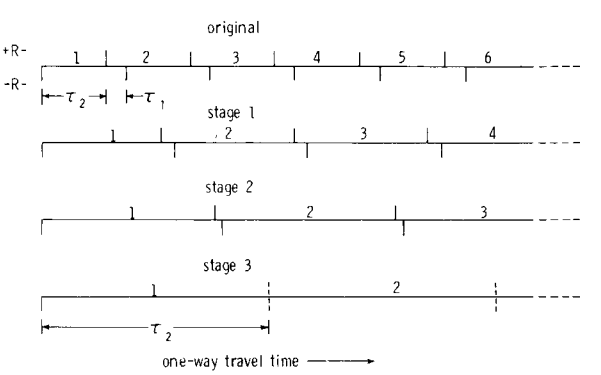


FIG. 20. Reflection coefficient time sequence for the original and each of the three stages of air-curtain configurations (Table 5).

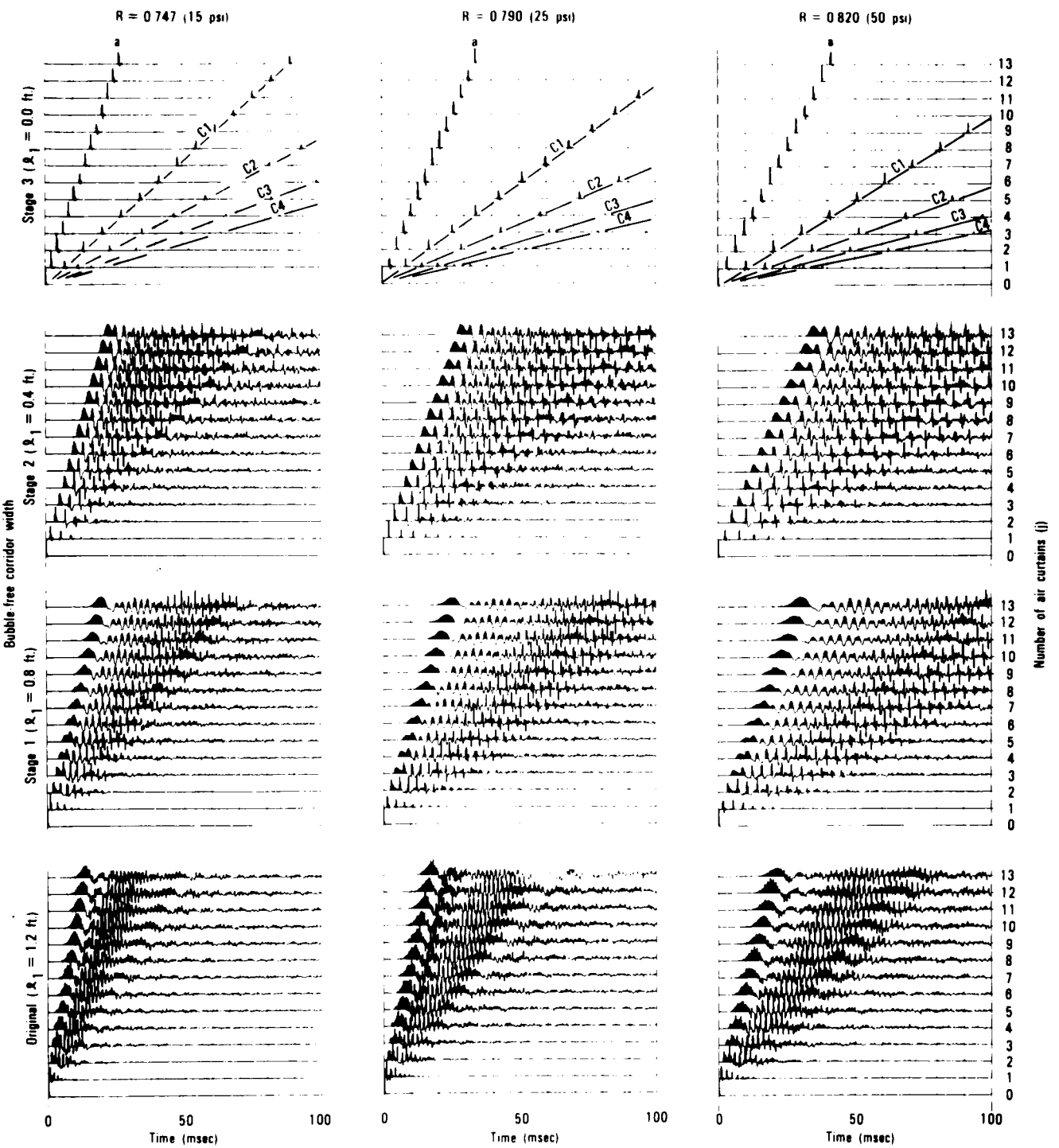


FIG. 21. Synthetic signals for each of four bubble-free corridor widths and each of three reflection coefficients $R$ corresponding respectively to the three air pressures. As in previous figures, each record is composed of traces for 0 through 13 air curtains.

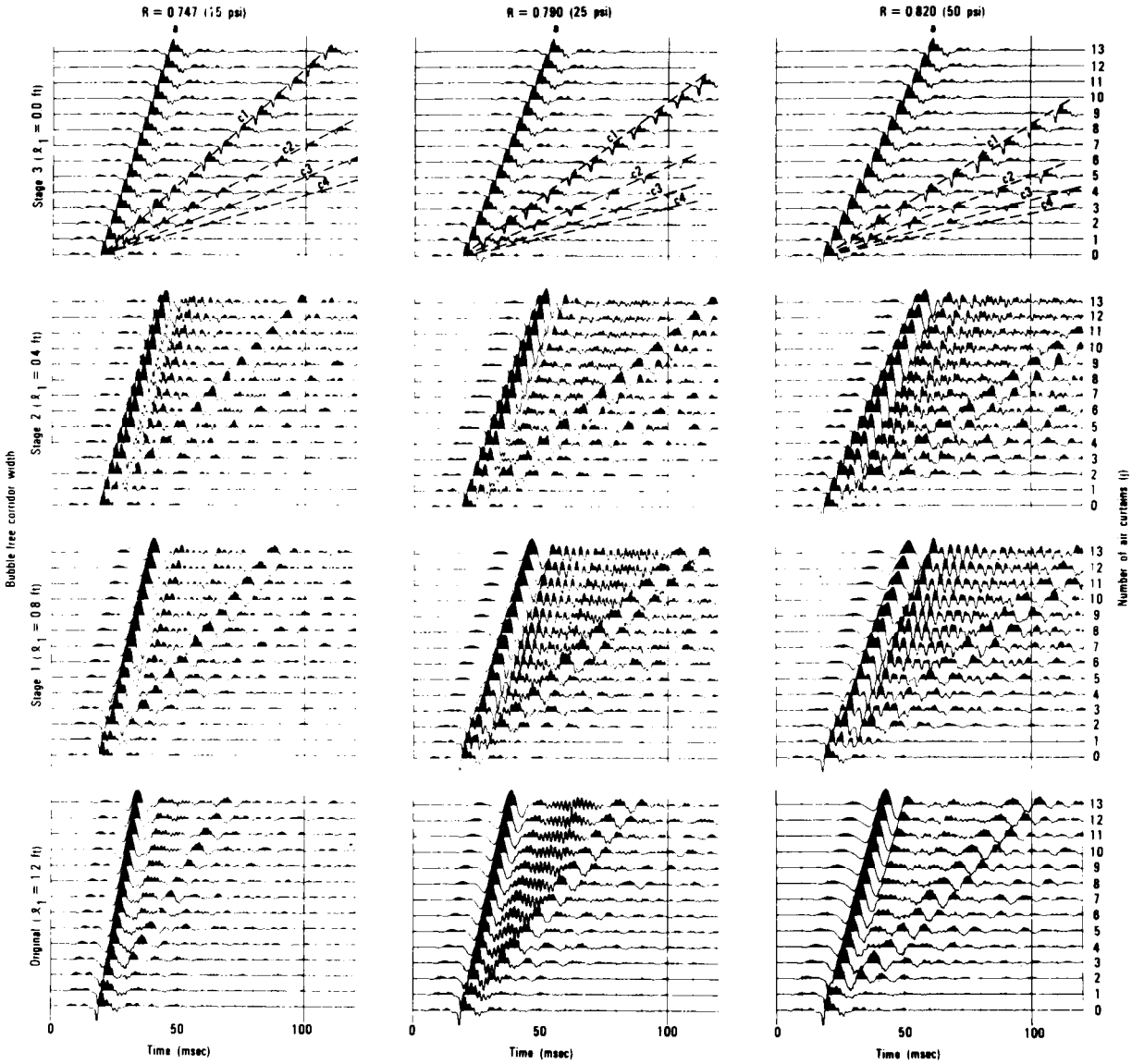


FIG. 22. Synthetic signals of Figure 21 convolved with a hydrophone 2 signal recorded without air curtains (bottom trace on each record).

Width $\ell_1$ of the bubble-free corridor was reduced to zero in increments of 0.4 ft from the original width of 1.2 ft by increasing the width $\ell_2$ of the air curtain by the same amount, as shown in Table 5. Velocity $c$ in the air curtain remained constant at values given in Table 2 for each of the three air pressures. The one-way traveltime $\tau_1$ in the bubble-free corridor and $\tau_2$ in the air curtain for each of three air pressures are listed in Table 5. Also given in Table 5 for reference are velocities $c$ in the air curtains and reflection coefficients $R$ from Table 2.

Reflection spike sequences were derived (Appendix A) for each bubble-free corridor width, commencing with the original ($\ell_1$ = 1.2 ft) and proceeding to stage 1 ($\ell_1$ = 0.8 ft), stage 2 ($\ell_1$ = 0.4 ft), and finally stage 3 ($\ell_1$ = 0.0 ft). The reflection coefficient time sequences for the original air curtain configuration and for each of the three stages are shown in Figure 20. At stage 3 (no bubble-free corridors), only the first ($-R$) and last ($+R$) spikes remain. As before, a synthetic trace was derived for no air curtains, and then traces were derived as successive air curtains up to 13 were added ($j$ = 0, 1, . . . , 13). The synthetic records are shown in Figure 21 in three sets of four records, a set for each air pressure (corresponding to a unique velocity and reflection coefficient) and a record for each air curtain configuration (original and three stages). The synthetic signals (reflection spike sequence), as before, are for plane waves and no absorption is applied. As the bubble-free corridor width is reduced, the signals are increasingly delayed due to the increased width of the low-velocity air curtain. The initial pulse (event a), which results from reverberations in the bubble-free corridors, is modified as the corridor width is reduced and becomes a single spike on each trace when these corridors are eliminated (stage 3). Also, the overall multiple reflections (Figure 16), identified as events c1, c2, etc., become single spikes upon elimination of the corridors. The synthetic signals of Figure 21 convolved with a hydrophone 2 signal recorded without air curtains are displayed in Figure 22. This convolution reduces the high-frequency content of the signals, and the first overall multiple (c1) is clearly visible on all records. Also, the effect of the bubble-free corridor width ($\ell_1$) on event a is obvious. As this width diminishes, event a becomes increasingly similar to the hydrophone 2 signal without air curtains (bottom trace on each record). At zero width (no corridors) the hydrophone 2 signal is unmodified on all traces, except for the time delay due to travel through the single air curtain.

Upon elimination of the bubble-free corridors, frequency-dependent absorption can be applied to the signals without ambiguity. The absorption $\alpha$ [equation (10), Domenico, 1982], in addition to frequency, depends upon bubble radius $r$ (Figure 9, Domenico, 1982) and fractional air volume $s$ (Figure 11, Domenico, 1982). The two extremes of bubble radius ($r$ = 0.002 and 0.014 ft) and the fractional air volumes (given in Table 4 from derived velocities) were assumed. For each combination of bubble radius and fractional air volume, and with the param-

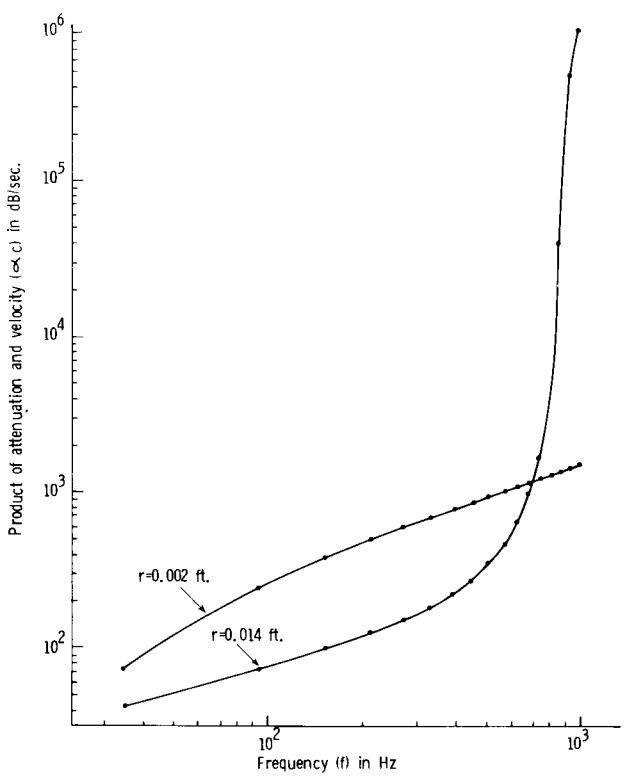


FIG. 23. Attenuation rate (dB/sec) versus frequency for an air-bubble/water mixture in which the bubble radius $r$ is 0.002 ft in one mixture and 0.014 in another mixture. Nominal fractional air volume is 0.005. Dots are at the center frequency of band-pass filters 60 Hz in width.

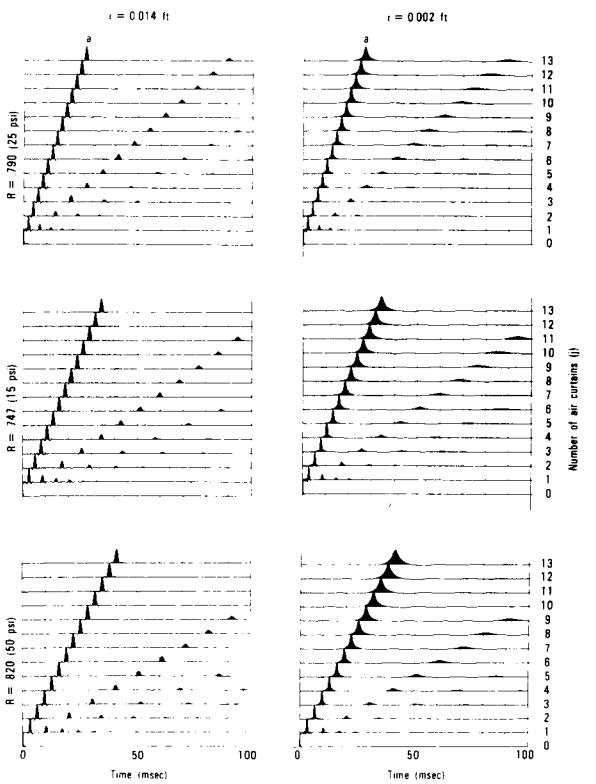


FIG. 24. Attenuation due to frequency-dependent absorption applied to synthetic records for coalesced air curtains (Figure 21, stage 3). Attenuation rates for a bubble radius $r$ of 0.002 ft and of 0.014 ft are plotted in Figure 23.

eters given in Table 1 of Domenico (1982) the absorption $\alpha$ and velocity $c$ were computed from equations (10) and (7) of Domenico (1982), respectively, over a frequency range extending from the minimum frequency limit to 1000 Hz. The product $\alpha c$ then gives attenuation in dB/sec, which is nearly invariant over the fractional air volume range considered ($s$ = 0.003 to 0.009). The product $\alpha c$ versus frequency is plotted in Figure 23 for $r$ = 0.002 ft and $r$ = 0.014 ft. The curve for $r$ = 0.002 ft is nearly linear, whereas the attenuation rate for $r$ = 0.014 increases rapidly in the upper frequency range as the resonant frequency is approached, greatly exceeding the rates for $r$ = 0.002. The time varying attenuation due to absorption was applied to the synthetic signals (Figure 21, stage 3) by first devising a succession of 17 band-pass filters 60 Hz wide and at center frequencies 60 Hz apart from 35 to 995 Hz. The center frequencies are indicated by dots on each of the two curves in Figure 23. The 17 filters were applied to each trace of the synthetic records, and the attenuation rate at the center frequency (Figure 23) of each filter was applied to the corresponding filtered component commencing at zero time. The final step was to sum the components of each trace, thereby approximating frequency and time varying attenuation. The resulting records for $r$ = .014 and $r$ = .002, and also for each of the three reflection coefficients $R$, are displayed in Figure 24. Amplitudes are normalized to the amplitude of the first pulse (event a). The frequency-dependent attenuation is evidenced by pulse broadening as the air-curtain width increases from zero to the overall width of 13 coalescing air curtains. Attenuation increasing with traveltime in the air curtain is evident from the reduction in amplitude of the overall multiples (events c1, c2, etc.) relative to event a. Also, the larger attenuation rates for a smaller bubble radius ($r$ = 0.002) over essentially the entire frequency range (Figure 23) are exemplified by the increase of pulse breadth on records for $r$ = 0.002 ft relative to that on records for $r$ = 0.014.

The amplitudes of event a on each record of Figure 24, normalized to the amplitude without air curtains ($j$ = 0), for $r$ = 0.014 ft and $r$ = 0.002 ft are plotted versus number of air curtains in Figures 25a and 25b, respectively. The attenuation for the smaller bubble becomes increasingly greater than that for the larger bubble as the air-curtain width increases (number of coalescing air curtains $j$ is increased). Also, the increase in attenuation with increase in reflection coefficient (due to increase in fractional air volume) is apparent. For comparison with these curves, the curves of event a amplitude measured on synthetic signals (Figure 18) for the original bubble-free corridor width ($\ell_1$ = 1.2 ft) are shown in both graphs. These are best aligned with the curves for the larger bubble (Figure 25a). Thus, it appears that attenuation of event a attributable solely to absorption (no bubble-free corridors) may be approximately equal to the attenuation attributable to reflection loss in bubble-free corridors. In the latter case, the traveltime in air curtains is negligible relative to traveltime in bubble-free corridors.

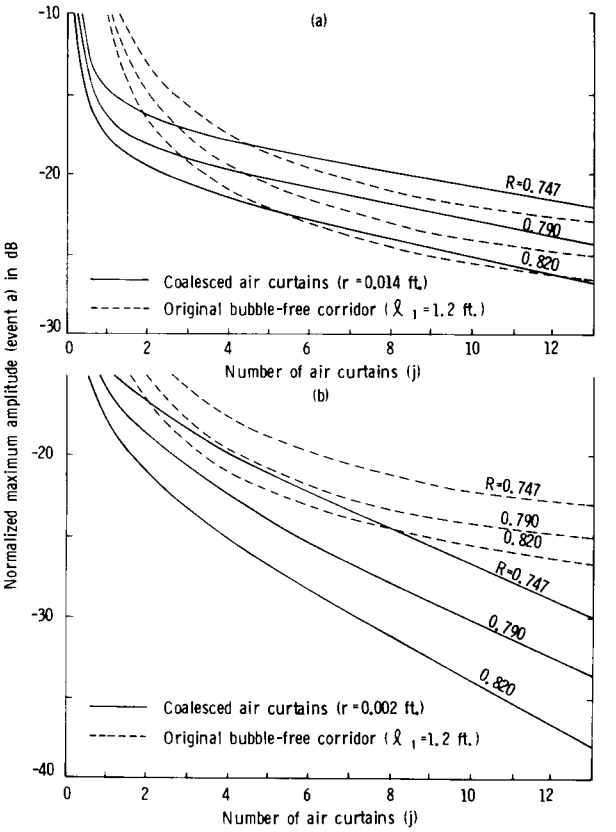


FIG. 25. Normalized event a amplitude versus number of air curtains, measured on records of Figure 24 for a bubble radius $r$ of (a) 0.014 ft and (b) 0.002 ft. Also shown on both graphs are event a amplitudes measured on synthetic signals (Figure 18) for the original bubble-free corridor width ($\ell_1$ = 1.2 ft).

## CONCLUSIONS

The field experiment consisted of hydrophone recordings in a pond, 25 ft deep, of signals transmitted through air-bubble curtains from a water gun source. The air curtains issued from one to 13 perforated pipes, at the bottom of the pond, 20 ft in length and spaced at intervals of 1.67 ft. Air pressures used were 15, 25, and 50 psi. Variation in response of the three hydrophones used in the experiment was reduced substantially by dividing the Fourier transform of each recorded signal by the transform of the signal recorded by the same hydrophone without air curtains, and then transforming the resulting spectra to obtain the time signals. The length and complexity of these signals indicate that reverberations occurred to an increasing extent as the number of consecutive air curtains was increased, demonstrating that bubble-free corridors existed between the air curtains. Analysis of the first positive pulse on the transformed signals indicates that time delay and reduction of the peak amplitude, and pulse broadening, as the number of consecutive air curtains increased, are attributable essentially to reverberations in the bubble-free corridors. The peak amplitude is decreased substantially by the first air curtain and remains at values of 0.1 to 0.2 of the peak value without air curtains (a delta function). The amplitude is not sensitive to air pressure; however, delay time of the peak amplitude, which increases linearly with number of air curtains, increases measurably with increase in air pressure.

Width of the bubble-free corridor, traveltime and velocity in the air curtain, and reflection coefficient at the interface of the air curtain and bubble-free corridor were determined by an iterative procedure, for each of the three air pressures, from signal onset times and delay times of the peak amplitude. The corridor width was approximately three times the air curtain width and did not

appear to vary with air pressure. On the contrary, traveltime in the air curtain increased with air pressure and was from three to four times the traveltime in the corridor. Correspondingly, velocity in the air curtain varied from about 0.14 to 0.10 times the velocity in bubble-free water (4870 ft/sec), and the associated reflection coefficients varied from about 0.75 to 0.82 with increase in air pressure. These characteristics were used to predict delay times of a latter positive pulse which, theoretically, should result from reverberations in the air curtains. They were also used to predict arrival times of multiple reflections between the outer interfaces of the outermost air curtains (overall multiples). The former cannot be identified, possibly because of energy absorption in the air curtains and interference from the first-order overall multiple. Second- and third-order overall multiples, however, are distinctive on various records and occur at nearly the predicted times.

Plane-wave synthetic signals, computed for each configuration of air curtains at each of the three air pressures, correspond satisfactorily to transformed hydrophone signals for the successive pipe sequence. Discrepancies are believed due to inadequacy of the synthetic signal computation (plane wave) and incomplete removal of hydrophone response. First pulse maximum amplitudes on the synthetic signals conform to those measured on the transformed recorded signals in that the amplitude is decreased substantially by a single air curtain and not appreciably more by additional air curtains. Also, as for the transformed signals, the first pulse maximum amplitude decreases with increase in air pressure. However, the amplitudes measured on the transformed signals exceed the synthetic signal amplitudes as the number of air curtains is increased, possibly due to the inadequacy of the plane-wave models for the synthetic signals and to unknown backscattered signals within the pond.

Fractional air volumes derived from air flow tests (measurements of pressure decline rate in air supply system at constant air pipe pressure) are from two to eight times greater than those given by the theoretical velocity versus fractional air volume function, the difference increasing with air pressure. This discrepancy may be due to an increase in bubble velocity (rate of rise) with increase in bubble production rate not accounted for in the reduction of air flow test data and, also, possibly due to variation in air-bubble density.

Presence of dominant reverberations in the bubble-free corridors between air curtains prevented meaningful measurements of frequency-dependent absorption in the air curtains. Alternatively, theoretical absorption values were obtained after synthetically eliminating the bubble-free corridors by expansion of the air curtains, maintaining a constant fractional air volume for each of the three air pipe pressures. Attenuation due to frequency-dependent absorption was determined for estimated upper and lower limits of bubble radius. (The effect due to variation of fractional air volume between established limits is negligible.) At the upper limit of bubble radius (0.014 ft), the first pulse (now the only signal except for separated overall multiple reflections) maximum amplitude is decreased substantially by the air curtain from a single pipe and at a much lower rate as successive air pipes are added. The frequency-dependent attenuation for the larger bubble radius closely approximates that due to reverberations in bubble-free corridors as determined from synthetic signals for the originally estimated air-curtain widths. Frequency-dependent attenuation determined for the smaller bubble radius (0.002) is substantially greater and increases with air-curtain width (addition of successive air pipes) at a greater rate.

## ACKNOWLEDGMENTS

The author is indebted to many individuals who provided invaluable assistance in the pursuit of the experiment reported here.

F. C. Haines, Jr., research engineer, Amoco Research Center, was responsible for design and construction of field equipment and assisted in preparation and performance of the field tests. Permission for use of Exxon Production Research Company's test pond at Friendswood, Texas, was given by J. B. Coffman, Exxon vice-president, Exploration. Arrangements for access to this facility were provided by R. H. Kirby, Exxon senior research engineer, who also arranged for operation of the Exxon recording equipment by Exxon research engineers G. R. Mathison and D. R. Young. Supervision of field equipment (air supply and perforated air pipe systems) construction in Houston was provided by W. H. Carmen, retired Amoco field foreman, who also coordinated, expedited, and supervised set-up and removal of this equipment. His services were arranged for by H. F. Patterson, Amoco Houston Region's operations geophysicist. P. E. Richardson, district manager, Birdwell Division of Seismograph Service Corp., provided hydrophones and auxiliary recording equipment, as well as assistance during the field test.

In the reduction of field data, the author is especially indebted to G. H. Neale, senior seismic analyst, Seismograph Service Corp., whose timely processing of data and ingenuity in program application were indispensable.

## REFERENCES

Christensen, R. E., Frank, J. A., and Geddes, W. H., 1975, Low-frequency propagation via shallow refracted paths through deep ocean unconsolidated sediments: J. Acoust. Soc. Am., v. 57, p. 1421–1426.

Domenico, S. N., 1979, Multiple reflections and head waves in the Gulf of Suez: Geophys. Prosp., v. 27, p. 539–563.

——— 1982, Acoustic wave propagation in air bubble curtains in water—Part I: History and theory: Geophysics, v. 47, this issue, p. 345–353.

Grant, F. S., and West, G. F., 1965, Interpretation theory in applied geophysics: New York, McGraw-Hill Book Co.

Hana, J. S., 1973, Short range transmission loss and the evidence for bottom-refracted energy: J. Acoust. Soc. Am., v. 53, p. 1686–1690.

Pekeris, C. L., 1942, The rate of rise and diffusion of gas bubbles in water: OSDR section no. C4-SR20, no. 326.

Thomson, W., 1950, Transmission of elastic waves through a stratified medium: J. Appl. Phys., v. 21, p. 89–93.

## APPENDIX A
## PLANE-WAVE SYNTHETIC SIGNALS

The physical model for derivation of plane-wave synthetic signals, shown in Figure A-1, basically is one-dimensional. It consists of alternating layers of bubble-free corridors and air curtains of thickness $\ell_1$ and $\ell_2$, respectively. Density and velocity in the bubble-free corridor are $\rho_0$ and $c_0$ and in the air curtain are $\rho$ and $c$, respectively. The development of plane-wave equations for computation of synthetic signals follows that given in Grant and West (1965, p. 85–88), based on a matrix formulation by Thomson (1950). The development is simplified considerably from that referenced because solid parallel layers of arbitrary thicknesses are replaced by alternating fluid layers of two types, specifically, the air curtain and the bubble-free corridor between air curtains, each of constant thickness, velocity, and density. Further simplification arises by having the plane wave parallel to the fluid layers.

As described previously, synthetic signals were derived for successive air curtains from one ($j = 1$) to thirteen ($j = 13$). For purposes of this treatment, the layers are numbered consecutively as shown in Figure A-1. Odd and even numbered layers are air curtains and bubble-free corridors, respectively. The first and last layers are always air curtains. Origin of the $z$-axis, perpendicular to the layers, is at the boundary between layer $n$ and $n - 1$. According to this nomenclature, then, the plane-wave pressure amplitude $A_{n-1}$ and displacement $W_{n-1}$ at $z = 0$, for boundary conditions of equal pressure and displacement, are given by

$$\begin{vmatrix} W_{n-1} \\ A_{n-1} \end{vmatrix} = \begin{vmatrix} 0 & -i\omega/c \\ -\omega^2\rho & 0 \end{vmatrix} \cdot \begin{vmatrix} D_n + E_n \\ D_n - E_n \end{vmatrix}, \quad \text{(A-1)}$$

where $D$ and $E$ are the advancing and reflected waves, respectively, and frequency $\omega = 2\pi f$. Similarly, the amplitude $A_n$ and displacement $W_n$ at $z = \ell_2$ are given by

$$\begin{vmatrix} W_n \\ A_n \end{vmatrix} = \begin{vmatrix} -(\omega/c)\sin\omega\tau_2 & -i(\omega/c)\cos\omega\tau_2 \\ -\omega^2\rho\cos\omega\tau_2 & i(\omega^2\rho)\sin\omega\tau_2 \end{vmatrix} \cdot \begin{vmatrix} D_n + E_n \\ D_n - E_n \end{vmatrix}, \quad \text{(A-2)}$$

where $\tau_2$ is one-way traveltime in the air curtain (layer $n$), and $i = \sqrt{-1}$. Inverting equation (A-1),

$$\begin{vmatrix} D_n + E_n \\ D_n - E_n \end{vmatrix} = \begin{vmatrix} 0 & 1/(\omega^2\rho) \\ i(c/\omega) & 0 \end{vmatrix} \cdot \begin{vmatrix} W_{n-1} \\ A_{n-1} \end{vmatrix}, \quad \text{(A-3)}$$

and substituting this into equation (A-2) we have

$$\begin{vmatrix} W_n \\ A_n \end{vmatrix} = \begin{vmatrix} \cos\omega\tau_2 & 1/(\omega c\rho)\sin\omega\tau_2 \\ -\omega c\rho\sin\omega\tau_2 & \cos\omega\tau_2 \end{vmatrix} \cdot \begin{vmatrix} W_{n-1} \\ A_{n-1} \end{vmatrix}. \quad \text{(A-4)}$$

In the same manner we may relate the amplitude $A_{n-1}$ and displacement $W_{n-1}$ at $z = -\ell_1$ to $A_{n-2}$ and $W_{n-2}$ by

$$\begin{vmatrix} W_{n-1} \\ A_{n-1} \end{vmatrix} = \begin{vmatrix} \cos\omega\tau_1 & 1/(\omega c_0\rho_0)\sin\omega\tau_1 \\ -\omega c_0\rho_0\sin\omega\tau_1 & \cos\omega\tau_1 \end{vmatrix} \cdot \begin{vmatrix} W_{n-2} \\ A_{n-2} \end{vmatrix}, \quad \text{(A-5)}$$

where $\tau_1$ is one way traveltime in the bubble-free corridor (layer $n - 1$). Then, designating the $2 \times 2$ matrix in equation (A-4) by $\mathbf{M}$ and that in equation (A-5) by $\mathbf{M}_0$ we have

$$\begin{vmatrix} W_n \\ A_n \end{vmatrix} = \mathbf{M} \cdot \mathbf{M}_0 \cdot \begin{vmatrix} W_{n-2} \\ A_{n-2} \end{vmatrix}, \quad \text{(A-6)}$$

or

$$\begin{vmatrix} W_j \\ A_j \end{vmatrix} = \mathbf{M}(\mathbf{M}_0\mathbf{M})^{j-1} \begin{vmatrix} W_0 \\ A_0 \end{vmatrix}, \quad \text{(A-7)}$$

where $A_0$ and $W_0$ are the amplitude and displacement at the plane wave source, and the index $n$ is replaced with the air curtain index $j$ (Figure A-1). The amplitude $A_j$ and displacement $W_j$ are those beyond the outer surface of the $j$th air curtain in a sequence of $j$ air curtains.

As a final step, the displacement must be replaced by the pressure amplitude. For the one-dimensional model employed here, these are related by the compressibility $\beta$ in the air curtain and $\beta_0$ in the bubble-free corridor. Only the latter is required in equation (A-7) since we are not concerned with recordings in the air curtains. Thus,

$$W_j = -\beta_0 A_j,$$

and

$$W_0 = -\beta_0 A_0.$$

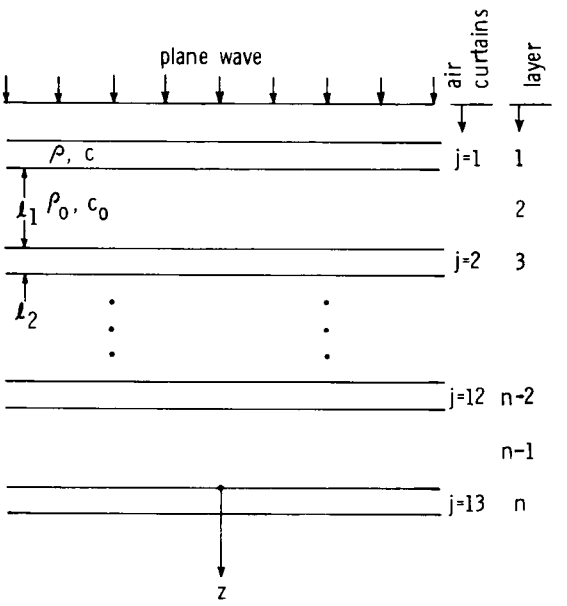


FIG. A-1. Model of air curtains and bubble-free corridors for computation of plane-wave synthetic signals. Density and velocity in the bubble-free corridors are $\rho_0$ and $c_0$, and in the air curtains are $\rho$ and $c$, respectively.

## APPENDIX B
## ANALYSIS OF WATER SURFACE AND WATER BOTTOM REFLECTIONS

Certain of the recorded signals provide an opportunity to determine the prominence of reflections from the water surface and water bottom in the absence of air curtains. The monitor hydrophone signals were recorded not only when this hydrophone was positioned near the water gun to monitor source signals, but also when it was positioned at a horizontal distance of 36 ft from the water gun with hydrophones 1, 2, and 3 for comparison of hydrophone responses (Figure 4). Thus, a monitor hydrophone signal recorded near the water gun may be convolved with a theoretical reflection spike sequence, representing the amplitudes and times of water surface and bottom reflections at a distance of 36 ft from the water gun, for comparison with the corresponding monitor hydrophone signal recorded at this distance.

Raypaths of the first eight reflections to arrive at the monitor hydrophone (M), a distance of 36 ft from the water gun, are shown in Figure B-1 on a vertical section of the pond. The raypaths occur in pairs of equal traveltimes since the hydrophone and

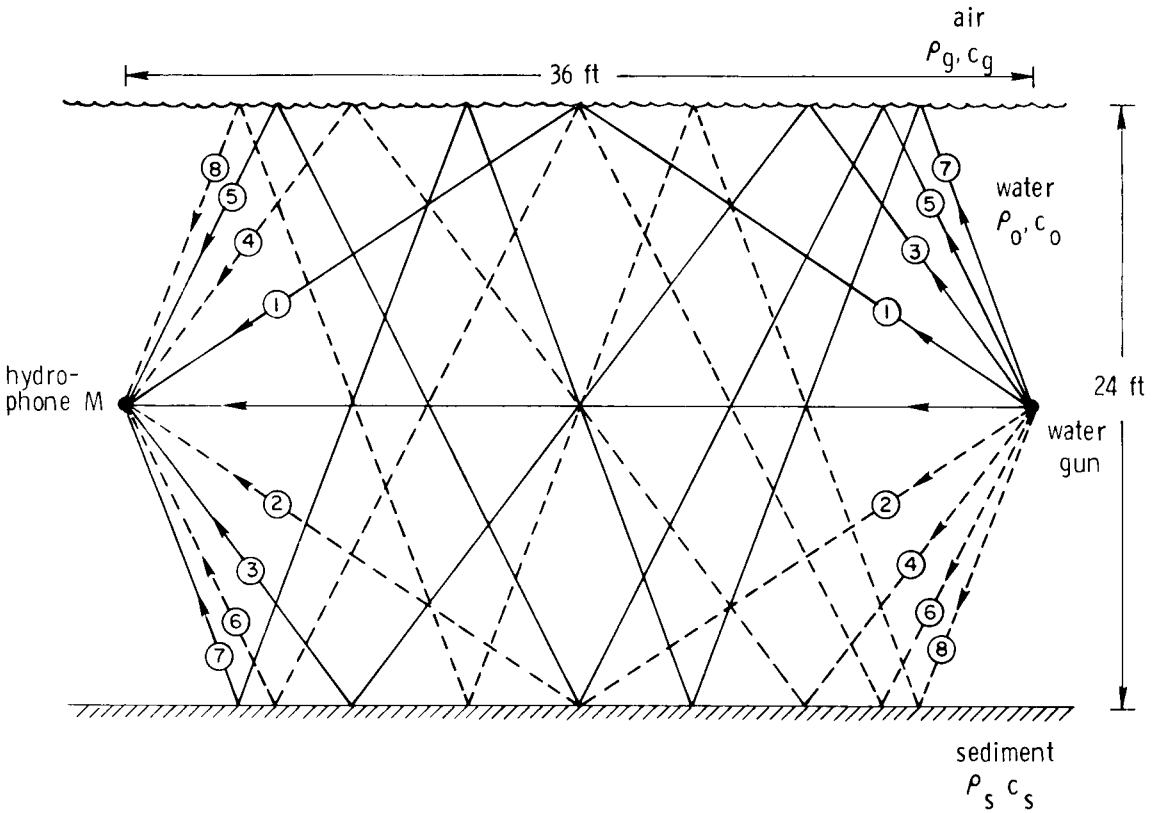


FIG. B-1. Reflection raypaths from the water gun to monitor hydrophone in the water pond. Only the first eight raypaths are shown.

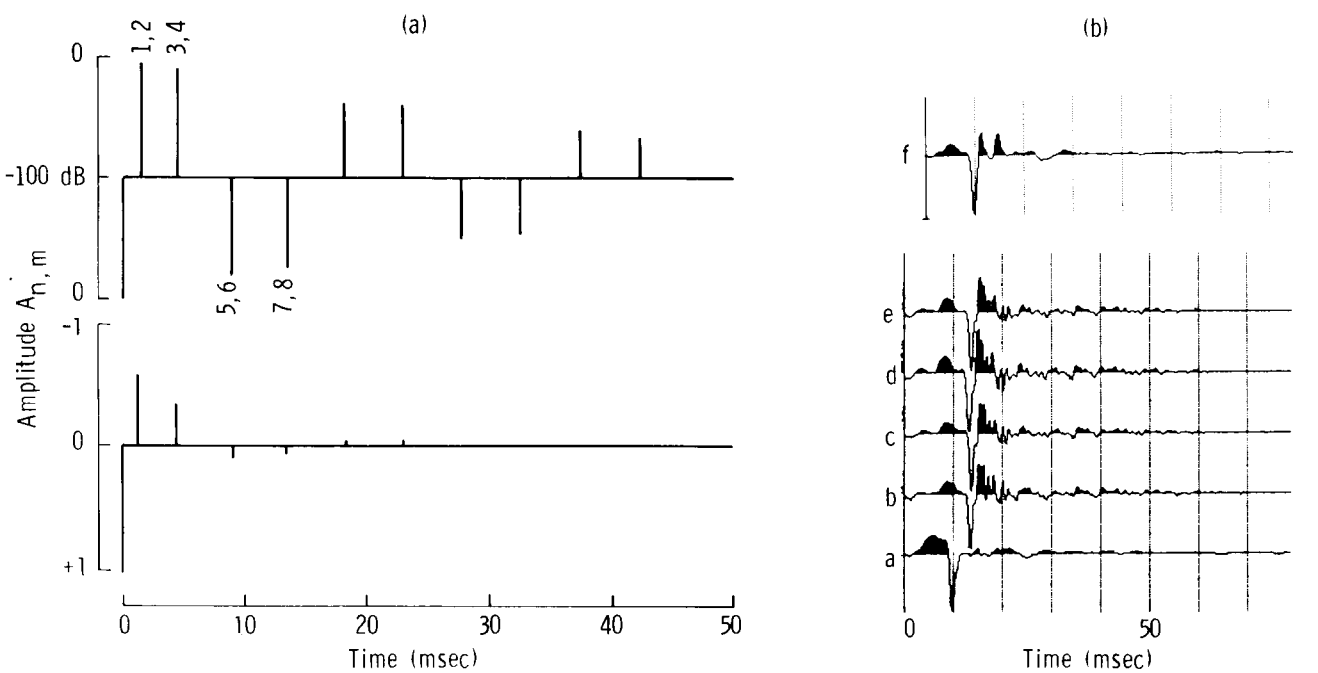


FIG. B-2. (a) Reflection spike sequence for reflections in the water pond between the water gun and monitor hydrophone (Figure B-1) and (b) monitor hydrophone signal recorded near the water gun (trace *a*) convolved with the reflection spike sequence (trace *f*) for comparison with monitor hydrophone signals recorded 36 ft horizontally from the water gun (traces *b*–*e*).

water gun are both at mid-depth. Traveltimes were obtained by determining raypath distances and dividing by the water velocity (4870 ft/sec). Reflection coefficients $R$ were derived from Grant and West (1965):

$$R = \frac{\frac{\rho}{\rho_0} - \frac{\sqrt{(c_0/c)^2 - \sin^2\theta}}{\sqrt{1 - \sin^2\theta}}}{\frac{\rho}{\rho_0} + \frac{\sqrt{(c_0/c)^2 - \sin^2\theta}}{\sqrt{1 - \sin^2\theta}}}, \qquad \text{(B-1)}$$

where $\rho_0$ and $c_0$ are, respectively, water density and velocity, $\rho$ and $c$ are density and velocity in the adjoining medium, and $\theta$ is the reflection angle. Because of the low density of air $\rho_g$ relative to density of water $\rho_0$, the ratio $\rho_g/\rho_0$ is negligible compared to the second term in the numerator and denominator of equation (B–1). Also, because of the low velocity in air $c_g$ relative to velocity in water $c_0$, the ratio $c_0/c_g$ is large compared to $\sin^2\theta$ for the reflection angles of the raypaths in Figure B-1 ($\theta \leq 30.3$ degrees). Thus, the reflection coefficient $R_g$ at the water surface reduces to $R_g = -1$. At the water-sediment interface it is assumed that the sediment velocity $c_s$ is equal to the water velocity $c_0$ as is usually the case for unconsolidated water bottom sediments (Christensen et al, 1975; Hana, 1973; Domenico, 1979). This sediment velocity implies that the fractional volume of water in the sediment is 0.5 and, assuming the remainder is quartz sand, that the density $\rho_s$ is 1.84 g/cm$^3$ (3.57 slugs/ft$^3$). For $c_s = c_0$, equation (B–1) reduces to simply

$$R_s = \frac{\frac{\rho_s}{\rho_0} - 1}{\frac{\rho_s}{\rho_0} + 1} \qquad \text{(B-2)}$$

and, as for $R_g$, $R_s$ is independent of the reflection angle $\theta$. The reflection coefficient $R_s$ of the water-sediment interface for the assumed sediment density $\rho_s$ and measured water density $\rho_0$ (Table 1 of Domenico, 1982) given by equation (B–2) is then 0.280.

The amplitude $A_{n,m}$ of a source signal recorded by the monitor hydrophone (Figure B-1) reflected $n$ times from the water surface and $m$ times from the water bottom, relative to the amplitude of the direct signal, is given by

$$A_{n,m} = \frac{36}{h} R_g^n R_s^m, \qquad \text{(B-3)}$$

where $h$ is the raypath distance in feet. Equation (B–3) was then used to compute the reflection spike sequence shown in Figure B-2a. The amplitudes are shown on a decibel scale and also on a linear scale. Raypaths in Figure B-1 corresponding to the first four spikes following the direct arrival are indicated by numbers in Figure B-2a. Amplitudes corresponding to raypaths beyond 3 and 4 appear to be negligible. The reflection spike signal was then convolved with a monitor hydrophone signal recorded near the water gun, shown on trace $a$ in Figure B-2b. The resultant signal is shown on trace $f$. For comparison with the latter, signals recorded by the monitor hydrophone positioned 36 ft horizontally from the water gun (Figure B-1) are shown on traces $b - e$. The derived signal matches the recorded signals reasonably well in that the initial upward pulse of the trace $a$ signal is diminished and that this signal is lengthened by the addition of two positive (upward) peaks following the principal trough. These two peaks are a result of the two raypath pairs 1, 2 and 3, 4.